When birds meet bauxite: Supergene Al-phosphate formation via guano infiltration in the Connétable Islands (French Guiana)

Jean de la Paix Izerumugaba, Beatrix Heller, Arnauld Heuret, Emilie Janots, Stéphane Schwartz, Alexandre Casanova, Geoffrey Aertgeerts, François Longueville, Rosella Pinna-Jamme, Thierry Allard, et al.

Ore Geology Reviews 193 (2026) 107280

Contents lists available at ScienceDirect

Ore Geology Reviews

journal homepage: www.elsevier.com/locate/oregeorev

When birds meet bauxite: Supergene Al-phosphate formation via guano infiltration in the Connétable Islands (French Guiana)

Jean de la Paix Izerumugaba [a,b,c], Beatrix Heller [a,d], Arnauld Heuret [b], Emilie Janots [a], Stéphane Schwartz [a], Alexandre Casanova [e], Geoffrey Aertgeerts [f], François Longueville [f], Rosella Pinna-Jamme [d], Thierry Allard [g], Sylvain Campillo [a], Sabine Sentenac [a], Cécile Gautheron [a,d,*]

[a] ISTerre, Université Grenoble Alpes, USMB, CNRS, IRD, UGE, 38000 Grenoble, France
[b] Géosciences Montpellier, CNRS, Université de Montpellier, Université de Guyane, France
[c] Université de Pau et des pays de l'Adour, CNRS, LFCR, IPREM, 64000 Pau, France
[d] Université Paris Saclay, CNRS, GEOPS, 91405 Orsay Cedex, France
[e] Département Formation et Recherche Sciences et Technologie, Université de Guyane, Cayenne 97300, Guyane, France
[f] BRGM, F-35700 Rennes, F-97333 Cayenne, France
[g] IMPMC, UMR CNRS 7590, Sorbonne Université, IRD, MNHN, 4 place Jussieu, F-75252 Paris Cedex 05, France

ARTICLE INFO

Keywords:
P-Alore deposit
Mineralogy
Laterite
Bauxite
Weathering
(U-Th)/He geochronology

ABSTRACT

The Grand Connétable (GC) and Petit Connétable (PC) Islands in French Guiana are iconic sites of geological heritage and hotspots of marine biodiversity. They are notable for their peculiar Al-phosphate deposits, which were previously exploited and are related to deep weathering profiles at sea level. Although the mineralogy of some Al-phosphate minerals has been described, there is no geological model for the formation of these weathering profiles and ore deposits. Therefore, we acquired geochemical, mineralogical, and geochronological data on the GC and PC islands to address this issue. Our findings revealed that the GC island, which rises up to ~ 70 m above sea level (a.s.l.), consists of a weathering profile exceeding 35 m in thickness, dominated by gibbsitic regolith (>30 m), and capped by an Fe-Al-P-duricrust. This bauxite deposit is thicker than those found on land in French Guiana, raising questions about the role of basement rock type, morphological factors, and ocean proximity in the development of bauxite deposits. The classic bauxitic profile at GC has recently been infiltrated by phosphoric acid from marine birds' guano derived. This has reacted with gibbsite to form rare Al-phosphate minerals such as variscite, *meta*-variscite and planerite, as well as Fe-phosphate minerals in a lower extent, down to the base of the profile. Ca-K-Al-sulphate minerals have been recognised to a lesser extent and can be traced back to the impact of sea spray in providing additional elements to the regolith. The PC Island, which is ~2 m high a.s.l. is made of a somital part of gibbsitic regolith, with only the Fe-Al duricrust is emerging. Hematite and goethite (U-Th)/He geochronology indicate that successive laterization (since the Oligocene) and bauxitization (since end of the Miocene) processes occurred in the area between ~30 and ~3 Ma, before the formation of the islands. The geochronological results are similar to those obtained from dated weathering profiles in French Guiana and Suriname, indicating a regional shift toward a more humid climate at the end of the Miocene. This information enables us to better define and discuss the Al-phosphate ore deposit over time, as well as its regional geological and paleoclimatic implications.

1. Introduction

Phosphorous is essential to all known forms of life and its importance as a fertiliser has long been recognised. However, phosphorous resources are limited across the globe, with the world's largest phosphorous reserves being found in phosphate rock, which occurs in large occurrences in North Africa. In South America, the use of guano (bird and bat excrement) as fertiliser dates back to pre-Columbian and even

* Corresponding author at: ISTerre, Université Grenoble Alpes, USMB, IRD, UGE, 38000 Grenoble, France.
E-mail address: cecile.gautheron@univ-grenoble-alpes.fr (C. Gautheron).

https://doi.org/10.1016/j.oregeorev.2026.107280
Received 9 November 2025; Received in revised form 30 March 2026; Accepted 15 April 2026
Available online 17 April 2026

pre-Inca times, as documented by early chroniclers and confirmed by recent studies (e.g. Santana-Sagredo et al. (2021) and references therein). Oceanic islands covered in seabird guano (known as "white gold") have been extensively exploited since the beginning of the 19th century to meet the agricultural industry's growing demand for phosphorous and nitrogen, both of which are contained in guano (Cushman, 2013). Control of guano resources has been a matter of high political interest and has been the source of international conflicts, such as the War of the Pacific (1879–1883). While guano exploitation initially focused on the Pacific coast of Central South America at the beginning of the 19th century, the search was soon extended to other regions of the Pacific and the Caribbean. In 1856, the United States passed the 'Guano Islands Act', which granted U.S. citizens who discovered a guano deposit on an unclaimed island exclusive to it (Skaggs, 1994).

One island that was exploited by American companies for its phosphorous resources is the Grand Connétable (GC), a small (220 × 170 m in size) Atlantic Island located around 15 km northeast of the coastline of French Guiana (Fig. 1A–B). Together with the neighbouring Petit Connétable Island (PC, 2 ha; Fig. 1C), it forms the nature reserve "Réserve Naturelle Ile du Grand Connétable", a sanctuary for marine birds and marine biodiversity (https://www.reserve-connetable.com). From 1882 to 1913, American companies extracted a total of 120,000 tonnes of phosphate from Grand Connétable Island leading to its current-man-made-cylindrical shape (Rostan, 2011; 2013) (Fig. 1D-F). Unlike typical island guano deposits in South America that are dominated by calcium phosphates (Schnug et al., 2018), the GC ore is unique

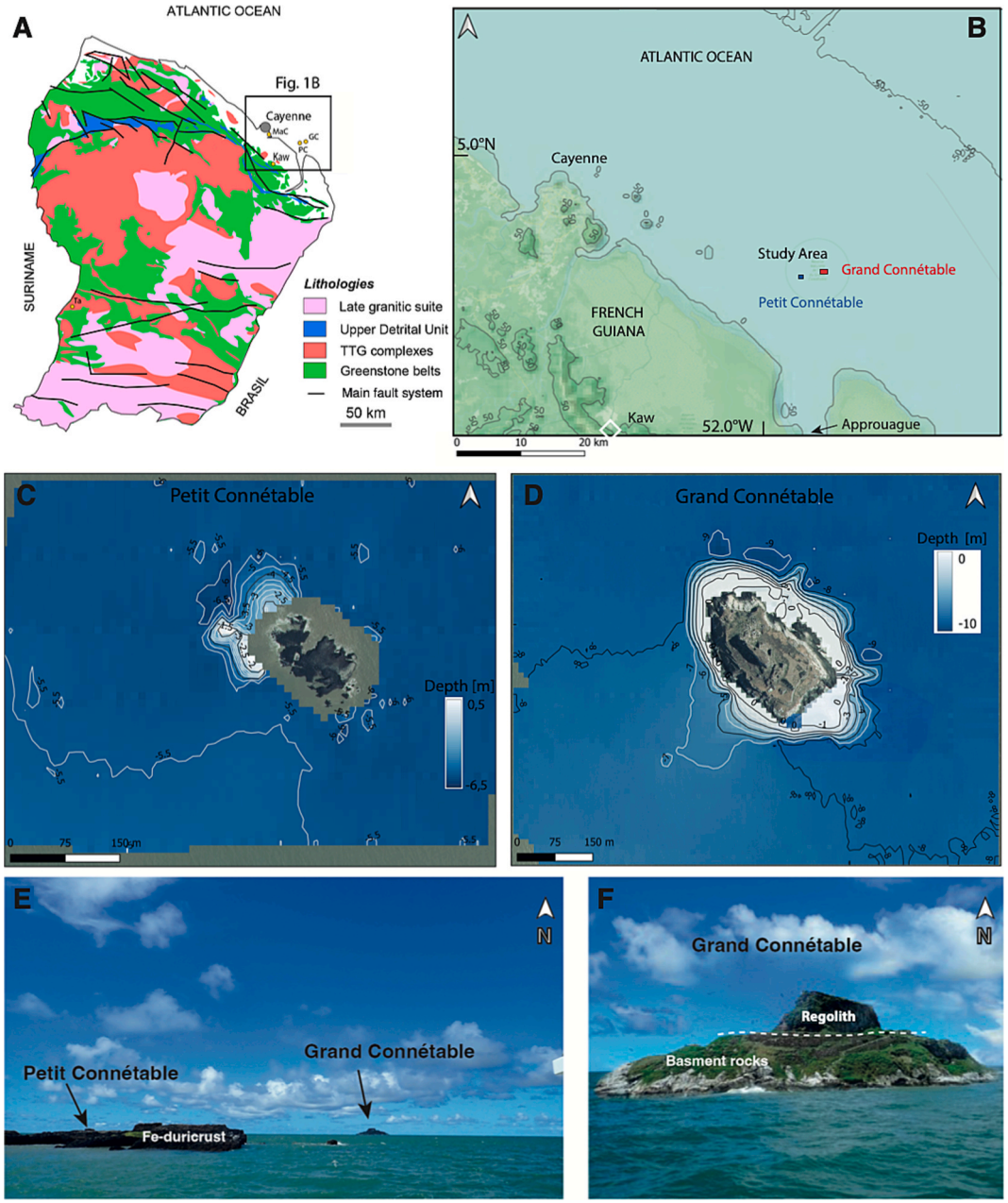

Fig. 1. Location of the Petit and Grand Connétable Islands. (A) Simplified geological map of French Guiana, with highlights: the Mahury Complex (MaC), the Tampoc Massif (Ta) and the area under study. The base map is based on Delor et al. (2003), and has been simplified by Eglinger et al. (2020). (B) Geographical location of French Guiana, focusing on the Cayenne area and showing the locations of the Kaw Mountains and the Petit and Grand Connétable Islands. it also shows the onshore and offshore bathymetry (GEBCO and OpenStreetMap). (C) and (D) underwater bathymetry of the Petit and Grand Connétable Islands respectively, obtained in October 2020. (E) A picture showing the ferruginous duricrust of the Petit Connétable Island and the Grand Connétable Island far to the north. (F) Picture of the present-day morphology of the Grand Connétable, with the dashed line representing the contact between the basement rock and the regolith.

in being composed of Al-phosphates (variscite and metavariscite among others) (Cautru et al., 1998) of unclear genesis occurring within a thick weathering profile, thereby forming a unique geological site (Longueville et al., 2021).

To shed light on the formation and evolution of the Connétable Islands and their unusual phosphate deposit, we conducted a mineralogical, geochemical and geochronological study, the results of which are presented in this contribution. Our results reveal that the islands consist of a thick lateritic bauxitic weathering profile that has developed on top of a yet undescribed anorthosite. Geochronological results from the lateritic to bauxitic cover enable us to relate the timing of the weathering at Connétable to events documented in nearby weathering profiles in French Guiana and Suriname. This improves our understanding of the regional paleoclimate and provides insight into the timing of island formation. Mineralogical analyses provide detailed documentation of the unique mineral assemblage found on the islands, enabling the development of a generic model of the Al-phosphates formed through the interaction of bird guano with bauxitic weathering products.

2. Regional context

2.1. Regional geology

French Guiana forms part of the Guiana Shield, which constitutes the northern block of the Amazonian Craton (South American Plate), which is dominated by a Proterozoic basement. This developed tectonically during the Transamazonian orogeny, of around 2.25–1.95 Ga, through collision and subduction-related metamorphism, as well as accretion, sedimentary processes and magmatism. These took place between older Archean rocks located in Venezuela, Brazil and Western Africa (Carozzi, 1979). The bedrock in French Guiana consists of low- to medium-grade metamorphic rocks, which formed through the deformation of greenstone belts and earlier calc-alkaline TTG (tonalite-trondhjemite-granodiorite) granitoids and tardi-orogenic granitic intrusions, and detrital unit (Delor et al., 2003), as illustrated on Fig. 1A. Apart from the southern part of the border with the Amazon Basin, the Guiana Shield is exempt of Paleozoic cover and is believed to have been above sea level at that time. It is a potential source of detrital Paleozoic sediments, which are only present in the Amazonas Basin (Carozzi, 1979; Grahn and Caputo, 1992).

The Guiana Shield is overprinted by extension-related features associated with the ~200 Ma Central Atlantic Magmatic Province (CAMP). This enhanced the opening of the North Atlantic and includes pluri-kilometric-length dykes (10–100 km long), rare sills, and basaltic flow remnants that filled the Amazon basin (Marzoli et al., 2017). The subsequent opening of the Atlantic Ocean led to the development of a passive margin during the Lower Cretaceous (120–100 Ma) (e.g., Basile et al., 2005; Sapin et al., 2016). Following the erosion of the passive margin, the rocks of French Guiana reached near-surface temperatures around 90 Ma (Derycke et al., 2021). No other major thermal event has affected the basement rocks in French Guiana, so no significant burial or erosion can be inferred. Apart from sedimentary deposits from the Upper Cretaceous to the Pleistocene, which are limited to a few coastal basins with an average thickness of around 50 m (e.g. Kroonenberg et al., 2019), but remain negligible in this context.

Plate tectonic reconstruction shows that the Guiana Shield has been in the intertropical zone since the Cretaceous (e.g., Nahon and Tardy, 1992) undergoing intense weathering under tropical conditions. This has resulted in lateritic and bauxite deposits ranging in thickness ranges from a few meters to 100 m (Tardy, 1992). Palynologically dated sedimentary archives, alongside paleomagnetic and (U-Th)/He ages determined on supergene minerals, suggest that the Guiana Shield has experienced episodic weathering since at least since the Eocene. A significant laterization episode occurred during the Oligocene, leaving well-developed deposits in French Guiana and Suriname (Ansart et al., 2022; Bardossy and Aleva, 1990; Heller et al., 2022; Monsels and Van Bergen, 2017, 2019; Théveniaut and Freyssinet, 2002; Van der Hammen and Wymstra, 1964; Wong, 1994). A Late Miocene to Pliocene bauxitization event has been recorded in French Guiana and Suriname, indicating a change in regional weathering conditions at that time (Ansart et al., 2022; Heller et al., 2022). Geomorphological studies proposing the development of paleosurfaces over the Guiana craton suggest that the age of laterite and bauxite formations is related to their elevation. These formations range in age from the Oligocene-Lower Miocene (>300 m a.s.l.) to the Quaternary (<150 m a.s.l.) (Blancaneaux, 1981; Choubert, 1957; Sapin et al., 2016). Sedimentological and geochronological studies show that coastal bauxite deposits in Suriname formed during the Late Eocene and Oligocene, when sediments were deeply weathered (Van der Hammen and Wymstra, 1964; Bardossy and Aleva, 1990; Wong, 1994; Monsels and Van Bergen, 2019). Basement rocks (~300 m. a.s.l.) where firstly lateritized forming in the Eocene to Oligocene, evolving through late Miocene bauxitization (Ansart et al., 2022; Heller et al., 2022; Théveniaut and Freyssinet, 1999; Théveniaut and Freyssinet, 2002).

2.2. The Grand and Petit Connétable Islands

The GC and PC islands are located approximately 15 km from the mouth of the Approuague River and 40 km south-east of Cayenne (Fig. 1B). PC Island is situated about ~ 3.4 km west of the GC Island (Fig. 1C and E). It is an isolated rock covering an area of around 2 ha with a low elevation (~2m a.s.l.) barely rising above sea level. It is completely of vegetation and is only used by migrating birds as a transit point (Fig. 1C and 2A-B). Longueville et al. (2021) proposed that the outcropping rock of the PC Island surface is an Fe-rich duricrust (Fig. 2B–C), but little is known about the regolith profile beneath it. The GC Island (Fig. 1D-F and 2D) measures 220 × 170 m in size, and is home to breeding shorebirds which have been depositing guano for years, resulting in a phosphate minerals resource. The phosphates were extracted by several American companies for fertilizer manufacturing from 1882 until 1913, when the resource was no longer economically viable (Rostan, 2013). The open-pit exploitation crafted the island's current geomorphology. Successive exploitation platforms have indeed been levelled into the initial rounded sugar loaf-shaped island, reshaping it into a sub-circular plateau, with a relatively small remaining rocky peak (~50 m high; about 400 m^2) in the middle. After 31 years of exploitation, this central rocky peak is the last remnant of the original phosphate deposit. According to macroscopic observations (Cautru et al., 1998), the main lithology of the Paleoproterozoic bedrock in the GC is leucocratic diorite, which is associated with amphibolite bodies. Cautru et al. (1998) found that the GC diorite is comparable to gabbro-dioritic bodies found in southern of Cayenne, which belong to the 'Mahury suite' as defined by Delor et al. (2003). One of these bodies has been dated at 2,144 ± 2 Ma (Théveniaut et al., 2006; Vanderhaeghe et al., 1998).

The GC Paleoproterozoic basement of the Guiana Shield is crosscut by a decametric N18-trending dolerite vein. At the scale of French Guiana, such Mesozoic dolerite veins with these orientations are related to the ~ 200 Ma Central Atlantic Magmatic Province (CAMP) (e.g., Nomade et al., 2002). Side-scan sonar data indicate the presence of rocky underwater extensions around the GC and PC, with low bathymetry (5–6 m b.s.l.), and these marine habitats constitute an important additional feature of the Grand Connétable National Natural Reserve (Longueville et al., 2021). The islands' basement rocks are heavily weathered and covered by a regolith over 30 m thick (Fig. 1F). From bottom to top, the weathering profile consists of a clay-rich fine saprolite containing phosphate-rich minerals and an Fe-Al duricrust. Several mineralised phosphate veins have been observed penetrating the entire profile have been observed (Fig. 1F).

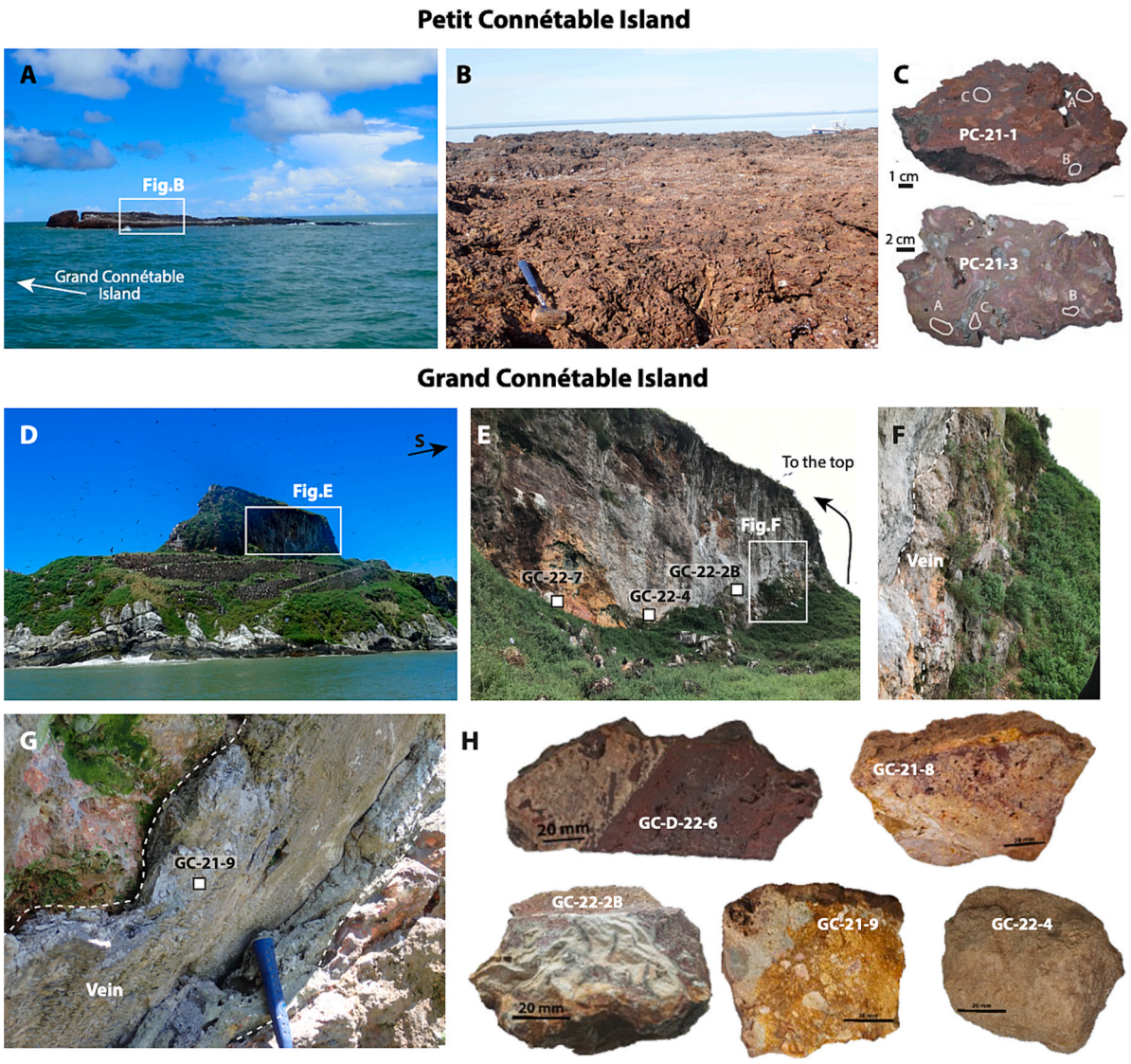

Fig. 2. Pictures of sampling on Petit and Grand Connétable Islands. (A) A general view of the Petit Connétable Island, (B) with a close-up of the duricrust and (C) pictures of the studied samples. (D) A general view of the Grand Connétable Island, with the bedrock capped by regolith. (E) The main accessible outcrop, sampled at the bottom. (F) and (G) show views of the filing white mineral veins observed at different positions within the regolith. (H) Selected pictures of the studied samples, presenting different typical facies.

2.3. Sampling

Due to its status as a natural wildlife reserve, access to GC is restricted, and circulation and sampling on the island are limited to a few paths, making extensive sampling challenging. Currently, guano is only present in limited quantities on the island, and no deposits have been observed at the sampling sites due to the intense rainfall washing any deposits into the sea (Fig. 1F). The samples studied in this work were collected during two sampling campaigns organized using the natural reserve's logistical resources and under the supervision of its staff. The first sampling campaign took place in 2021, providing 10 samples from GC ("GC21" samples) and 2 samples from PC ("PC21"). The second campaign, in 2022, provided a further 14 samples from GC ("GC22").

Samples of different GC lithologies were collected from various locations on the island (Figs. 2-3 and Table 1). Samples were collected at various elevations from different parts of the weathering profile. These included mineralised hard phosphate materials of various colours and internal structures, as well as boulders of Fe-Al-P duricrusts (Fig. 2H). This is because no Fe-Al-P duricrust samples were observed on the island's surface due to its strong reworking during exploitation. Additionally, the sample set includes 3 samples of the fresh bedrock: one sample of the Proterozoic-dominant diorite lithology (as defined by Cautru et al., 1998), one sample of a Paleoproterozoic rock, and one sample of dolerite dyke rock. As the ferruginous duricrust was the only lithology present, it was the only one sampled at the PC island, where 2 samples were collected. Table 1 contains the sampling coordinates and elevations, as well as short descriptions of the 26 samples studied in this work. Figures. S1 and S2 show pictures of the samples (supplementary materials).

3. Methods and data

3.1. Sample preparation

First, the samples were cut into slices using a steel saw to enable macroscopic petrological observations and photography. One representative piece of each sample was crushed to less than 2 mm using a metal mortar and then ground into a fine powder for bulk mineralogical and geochemical analyses. For further mineralogical and geochronological analyses, subsamples were separated from the slices and

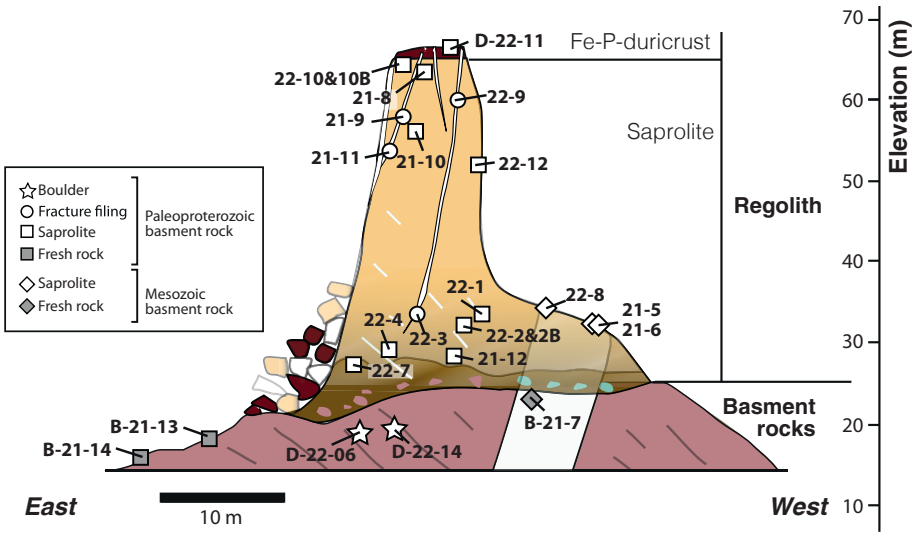

Fig. 3. The positions of the samples studied in this work are shown on the Grand Connétable regolith profile, from the basement to the duricrust. The geological cross-section and descriptions of the Grand Connétable Island are taken from Cautru et al. (1998). All sample names start with 'GC'. For basement rock samples, the prefixes B- and D- indicate in-place basement and boulder duricrust samples, respectively.

prepared according to the methods described in sections 3.2. and 3.4.

3.2. Mineralogical analysis

XRD analyses were performed at the ISTerre laboratory (Université Grenoble Alpes, France) and acquired on 1 g of bulk sample fractions using a Bruker D8 powder diffractometer equipped with a SolXE Si (Li) solid-state detector from Baltic Scientific Instruments, using CuKα_1 + 2 radiation. The XRD analysis acquisition time was set to 8 h to obtain well-defined peaks and to reduce the fluorescence interference from iron-rich samples. The mineral phases were identified using the PANalytical HighScore software followed by a Rietveld refinement for quantification (McCusker et al., 1999). The associated error bars are 1% for crystallized phases. The XRD data are reported in Table 2. Subsamples were manually separated to create polished studs for SEM micrographs and further mineralogical observations including BSE (backscattered electron) imaging and EDS (energy dispersive spectroscopy). SEM analyses were performed on carbon-coated samples using a conventional TESCAN VEGA-3 SEM equipped with a RAYSPEC EDS detector (SSD 30 mm^2 2152).

3.3. Major and trace elements composition

For most samples, the major element composition data were obtained from 1-2 g of bulk sample fractions analysed at the Service d'Analyse des Roches et des Minéraux (SARM) in Vandoeuvre-Les-Nancy, France, using an ICP-OES iCap6500. A detailed description of the analytical protocol used at SARM can be found at www.sarm.cnrs.fr. Only sample GC21-06 was analysed at ISTerre using an ICP-AES (Varian, model 720ES), after dissolution accordingly to the protocol developed by Wiggenhauser et al. (2021). Based on observed and reported petrology, and on bulk and pinpoint mineralogical data, the following 10 major elements were analysed for: Al, Ca, Fe, K, Mg, Mn, Na, P, Si, and Ti. The major element composition data are presented in Table 3, expressed in oxide wt% (i.e., Al_2O_3, CaO, Fe_2O_3, K_2O, MgO, MnO, Na_2O, P_2O_5, SiO_2 and TiO_2 respectively). Table 4 reports the results for trace and rare earth elements.

3.4. (U-Th)/He geochronological analysis

The (U-Th)/He geochronological analysis was conducted on the PC duricrust in the same way as in Heller et al. (2022) to avoid any phosphate contamination. Two blocks of duricrust were collected and sawed, and 3 to 4 sub-samples were extracted from the inner parts of each sample using a Dremel multitool (Fig. 2C). Optically pure hematite and goethite fragments were then selected from these sub-samples under a binocular microscope. For age dating, a total of 31 single hematite and goethite fragments, measuring ~100–600 μm and weighting 16–236 μg, were encapsulated in weighed niobium (Nb) tubes. The He content was measured at the GEOPS laboratory (Université Paris Saclay, France) using an He extraction and purification line coupled with a quadrupole mass spectrometer (Gautheron et al., 2021). After degassing, the Nb tubes were placed directly into 5 ml Teflon-capped vials for complete dissolution in a HNO_3 acid solution containing a known amount of ^{235}U, ^{230}Th, and ^{149}Sm, in accordance with the protocol described in Verhaert et al. (2022). U, Th, and Sm measurements were undertaken by using an ELEMENT XR ICPMS at the GEOPS laboratory. The raw (U-Th)/He age was corrected for He diffusional loss following the prediction of Bassal et al. (2022) for goethite and Heller et al. (2022) for hematite. The (U-Th)/He data are reported in Table 5.

4. Results

4.1. Bulk mineralogy

Fig. 4 shows the X-ray diffractograms obtained from the bulk GC regolith samples of the GC studied in this work. Table 2 presents the complete mineralogical composition. The samples of the regolith taken from both the rock matrix and from filled fractures are dominated by gibbsite ($Al(OH)_3$) and alumino-phosphates, specifically the two polymorphs variscite and metavariscite ($Al(PO_4).2H_2O$), as well as planerite ($((Cu_{0.23}(H_2)_{0.77})_{1.00}Al_{5.97}(PO_4)_{4.00}(OH)_{7\cdot91}4H_2O)$) (Matsubara et al., 1988) (Fig. 4). Two samples taken from the lower part of the profile are rich in kaolinite ($Al_2Si_2O_5(OH)_4$). Notably, sample GC22-01 consists of 67% kaolinite, and sample GC22-04 consists of 99% kaolinite (Fig. 4). Sample GC21-13 shows that the Paleoproterozoic basement is dominated by plagioclase (62%), alongside greenschist metamorphic minerals namely epidote, chlorite and vermiculite (27%), as well as 6% of amphibole, indicating an anorthosite-like mineralogy. Sample B-GC21-14 shows that the less common amphibolite mainly consists of amphibole (72%), plagioclase (18%), quartz (8%) and epidote (<3%), matching the previously reported amphibolite lithology. The Mesozoic dolerite intrusion basement (GC21-07) consists of plagioclase (50%), pyroxene (29%), and some other phases (Table 2).

Table 1
List of studied samples, with location coordinates, elevation of sampling locations, and short descriptions.

Sampling names	Used names	Latitude (°N)	Longitude (°W)	Elev. (m)	Description
PC-21-01	GC21-01	4.8179083	−51.967683	2	Fe-Al-duricrust
PC-21-03	GC21-03	4.8179083	−51.967683	2	Fe-Al-duricrust
GC-21-05	GC21-05	4.824850	−51.936417	40	Fine Saprolite, matrix
GC-21-06	GC21-06	4.824850	−51.936417	40	Guano-rich
GC-B-21-07	GC21-07	4.824983	- 51.936467	60	Mesozoic Dolerite bedrock
GC-21-08	GC21-08	4.825317	−51.936967	71	Fine Saprolite_matrix
GC-21-09	GC21-09	4.825117	−51.936700	64	Fracture- filling vein; phosphates
GC-21-10	GC21-10	4.825100	−51.936717	63	Regolith_matrix
GC-21-11	GC21-11	4.825050	−51.936567	59	Fracture- filling vein; phosphates
GC-21-12	GC21-12	4.824950	−51.936683	41	Regolith_matrix
GC-B-21-13	GC21-13	4.826100	−51.936767	21	Paleoproterozoic bedrock
GC-B-21-14	GC21-14	4.826050	−51.936983	15	Paleoproterozoic bedrock
GC-22-01	GC22-01	4.825039	−51.936735	36	Regolith, base of weathered Profile
GC-22-02	GC22-02	4.825219	−51.936631	35	Hematite red; Regolith; nodule
GC-22-02B	GC22-02B	4.825219	−51.936631	35	Hematite + phosphates, Regolith
GC-22-03	GC22-03	4.825258	−51.936772	35	Fracture-filling vein; phosphates
GC-22-04	GC22-04	4.825277	−51.936832	33	Regolith_matrix; Kaolinite
GC-D-22-06	GC22-06	Boulder			P-Al-Fe Duricrust
GC-22-07	GC22-07	4.825491	−51.936860	32	Fine Saprolite_matrix
GC-22-08	GC22-08	4.824685	−51.936477	41	Fine Saprolite_matrix
GC-22-09	GC22-09	4.825045	−51.936679	58	Fracture-filling vein; phosphates
GC-22-10	GC22-10	4.825053	−51.936672	62	Peak_Fine Saprolite_matrix
GC-22-10B	GC22-10B	4.825053	−51.936672	62	Peak_Fine Saprolite_matrix
GC-D-22-11	GC22-11	4.825292	−51.936944	64	Peak_duricrust
GC-22-12	GC22-12	4.824999	−51.936492	52	Fine Saprolite_matrix
GC-D-22-14	GC22-14	Boulder			P-Al-Fe duricrust

Fig. 5 shows the mineralogical composition of the GC regolith rock matrix samples as a function of elevation, based on the main mineralogical phases determined by XRD. P-Al-Fe duricrust samples were placed on top of the regolith, even though they were initially collected as boulders at lower elevation. Neither the fracture-filling vein samples nor the dolerite-developed regolith samples were included, as the former are likely to introduce a high phosphor-infiltration-related bias into the mineralogy, and the latter only represent a very small part of the GC. Al-phosphate minerals were observed throughout the section but were much more abundant in the duricrust. Iron oxides and hydroxides were also more concentrated in the duricrust. Gibbsite dominated the rest of the regolith, and kaolinite was only observed at the base of the regolith profile.

For the PC Fe-duricrust samples (D-PC21-1 and −3) the bulk mineralogy is very similar, consisting mainly of hematite (45 and 52 wt %), goethite (30 and 33 wt%), and gibbsite (17 and 20 wt%). Small amounts of anatase, boehmite, and rutile are present, whereas kaolinite and quartz were not detected in these samples (Table 2). Based on the XRD data and Rietveld adjustment, Al-substitution in the goethite of the PC samples has been determined, yielding significant amounts of ~7 and 17 mol%.

4.2. Macroscopic and microscopic sample petrology and mineralogy

The macroscopic petrology of the PC and GC samples has been determined, with inputs of mineral species identified using the SEM (Fig. S3). Figures. S1 and S2 (supplementary section) show further images of the GC samples. The mineral types were characterized using phase colour (e.g., red for hematite and orange for goethite), XRD-based mineralogy, and SEM analyses. The Fe/Al duricrust consists of mostly massive, but sporadically porous, red (GC22-11) to dark red (GC22-06), mostly iron(III) oxide matrix, which is filled with pale green to white, or yellowish brown variscite (Var or metavariscite), and may contain clasts of hematite (Hem) (GC22-06). The gibbsite (Gbs) zones exhibit various porosities, ranging in colour from yellowish light (GC21-08 and 10) to brown (GC21-09), with occasional dark brown to red patches of pure iron oxides and oxyhydroxides (GC21-08), or solid solutions series of Al and Fe and/or P (GC21-09). The GC21-09 matrix contains reworked clasts of aluminium hydroxide (mostly gibbsite with boehmite to a lesser extent). Variscite (or metavariscite) is most prominent in samples of fracture-filling samples, where it appears as fine-grained, non-porous, ranging in colour from pale green to greyish white (GC21-09 and veinlets in GC21-11) or as coarse grained, porous and grey to brown (matrix of GC21-11). The kaolinite (Kln), which is located at the bottom of the saprolite is fine-grained, sticky, plastic, and yellowish-brown. The kaolinite levels contain dozens of centimetre-sized, clay-rich nodules coated in fine-grained hematite. By contrast, the Proterozoic and Mesozoic basement samples display a phaneritic texture dominated by light-coloured minerals (over 80% in GC21-13). These samples are fine-grained and contain a high proportion (~ 50%) of dark minerals (GC21-14 and 07), as shown in Supplementary section Fig. S3.

Additionally, the samples collected during the first fieldtrip campaign were examined using a SEM-BSE to conduct a detailed mineralogical analysis. Selected samples (G21-08, -09 and -10) are presented in Fig. 6 for illustration. Further images of samples G21-05, −11 and −12 can be found in Fig. S4 (supplementary material). The regolith samples mostly exhibit fine-grained homogeneous mineral phases of Al-phosphate and Al-hydroxide in different intensities of grey, with occasional, predominantly small, grain-like white phases of Ti and Fe oxides (Fig. 6). As they are polymorphs, variscite and metavariscite cannot be differentiated using an SEM; therefore, all phases corresponding to $Al(PO_4).2H_2O$ are referred to as variscite (Var) in this section. Solid solution series phases containing varying concentrations of Al, P, and Fe (which cause a macroscopically visible red-rust coloration) were identified in samples GC21-09, GC21-12, and GC21-08. Sample GC21-09 contains reworked clasts of gibbsite and variscite contained within the matrix of a solid solution series ($Al_3FeP_5O_8$) and variscite. A pure phase of strengite ($FePO_4{\cdot}2H_2O$) was found in sample GC21-05 present as both as a fine-grained matrix and fibrous shaped, growing within the porosity (Fig. S4), through it was not identified by XRD. Pisoid crystalline variscite was also observed to be growing within the porosity of samples GC21-05 and GC21-12. The latter sample also shows a new calcium sulphate-rich phase that was not identified by XRD (Fig. S3). Fig. 6 and S4 show the BSE-determined mineralogy of the regolith.

For the Petit Connétable samples, different phases of hematite and goethite have been distinguished, based on colour, in addition to gibbsite (Fig. 2).

Table 2
Mineralogical content (%) of the studied samples was determined using Rietveld refinement of the XRD spectrum. The respective empirical formulas are given in Table S1 of the supplementary materials.

Mineral	1stsamplingcampaign(PC21−)		1stsampling campaign (GC21−)									2ndsampling campaign (GC22−)													
Sample	*01*	*03*	*05*	*07*	*08*	*09*	*10*	*11*	*12*	*13*	*14*	*01*	*02*	*02B*	*03*	*04*	*06*	*07*	*08*	*09*	*10*	*10B*	*11*	*12*	*14*
Alt (m)	*2*	*2*	*40*	*30*	*61*	*54*	*53*	*49*	*31*	*21*	*15*	*36*	*35*	*35*	*35*	*33*		*32*	*41*	*58*	*62*	*62*	*64*	*52*	
Primary minerals																									
Plagioclase	–	–	–	49.8	–	–	–	–	–	37.1	–	–	–	–	–	–	–	–	–	–	–	–	–	–	–
Labradorite	–	–	–	–	–	–	–	–	–	–	17.9	–	–	–	–	–	–	–	–	–	–	–	–	–	–
Bytownite	–	–	–	–	–	–	–	–	–	24.9	–	–	–	–	–	–	–	–	–	–	–	–	–	–	–
Clinozoisite	–	–	–	–	–	–	–	–	–	12.7	–	–	–	–	–	–	–	–	–	–	–	–	–	–	–
Zoiste	–	–	–	–	–	–	–	–	–	10.4	–	–	–	–	–	–	–	–	–	–	–	–	–	–	–
Chlorite	–	–	–	–	–	–	–	–	–	4.0	2.5	–	–	–	–	–	–	–	–	–	–	–	–	–	–
Vermiculite	–	–	–	–	–	–	–	–	–	–	–	–	–	–	–	–	–	–	–	–	–	–	–	–	–
Arfvedsonite	–	–	–	–	–	–	–	–	–	6.3	–	–	–	–	–	–	–	–	–	–	–	–	–	–	–
Amphibole	–	–	–	–	–	–	–	–	–	–	72	–	–	–	–	–	–	–	–	–	–	–	–	–	–
Augite Px	–	–	–	28.8	–	–	–	–	–	–	–	–	–	–	–	–	–	–	–	–	–	–	–	–	–
Lizardite	–	–	–	4.5	–	–	–	–	–	–	–	–	–	–	–	–	–	–	–	–	–	–	–	–	–
Quartz	–	–	–	4.3	2.8	–	–	0.73	–	4.5	7.6	–	–	0.6	3.5	–	–	–	–	–	–	–	–	–	–
Cristobalite	–	–	–	–	–	–	–	–	–	–	–	–	–	–	–	–	–	2.4	–	–	–	–	–	–	–
Al hydroxides																									
Gibbsite	17.3	20.3	–	1.5	94.5	81.8	69.3	3.2	75	–	–	1.9	–	–	–	0.7	–	97.6	–	74.6	100	81.0	79.7	70	–
Boehmite	0.3	0.3	–	–	–	0.8	–	–	–	–	–	–	–	–	–	–	–	–	–	–	–	–	–	–	–
Clays																									
Dickite (kln)	–	–	–	–	–	–	–	–	–	–	–	–	–	–	–	45.8	–	–	–	–	–	–	–	–	–
Kaolinite	–	–	–	1.8	–	–	–	–	7.6	–	–	67.0	1.9	–	–	53.5	–	–	–	–	–	–	–	–	–
Al, Fe and Ti phosphates and sulphates																									
Variscite ($AlPO_4{\cdot}2H_2O$)	–	–	34.7	–	–	6.4	25	59.5	–	–	–	15.6	39.2	44.3	42.2		34.9	–	33.0	7.3	–	7.4	5.8	–	49.1
Metavariscite ($AlPO_4{\cdot}2H_2O$)	–	–	59.7	–	–	–	–	36.5	–	–	–	11.0	33.8	43.6	44.3	–	40	–	49.2	–	–	–	–	–	41.0
Planerite $(Cu_{0.23}(H_2)_{0.77})_{1.00}Al_{5.97}(PO_4)_{4.00}(OH)_{7.91}{\cdot}4H_2O$	–	–	–	–	–	–	–	–	11.1	–	–	–	–	–	–	–	–	–	4.8	18.1	–	11.6	–	20.8	–
Titanium phosphate (TiP_2O_7)	–	–	–	–	–	–	–	–	–	–	–	–	–	1.4	0.8	–	–	–	–	–	–	–	–	–	1.5
Heterosite ($FePO_4$)	–	–	–	–	–	–	–	–	–	–	–	1.7	–	–	–	–	–	–	–	–	–	–	–	–	–
Calcium Sulfoaluminate ($Ca_4Al_6O_{12}SO_4$)	–	–	–	–	–	–	–	–	–	–	–	–	–	3.2	3.4	–	4.1	–	–	–	–	–	–	–	3.1
Alunite ($KAl_3(SO_4)_2(OH)_6$)	–	–	–	–	–	–	–	–	–	–	–	–	–	–	–	–	–	–	–	–	–	–	11.1	–	–
Fe and Ti oxides and hydroxides																									
Hematite	51.7	45.1	–	–	1.4	–	5.7	–	0.43	–	–	2.0	25.2	7	5.8	–	20.7	–	11.1	–	–	–	3.5	–	5.3
Maghemite	–	–	–	–	–	–	–	–	–	–	–	–	–	–	–	–	–	–	–	–	–	–	–	1.5	–
Goethite	30.0	32.9	–	–	1.2	10.0	–	–	5.9	–	–	0.7	–	–	–	–	–	–	–	–	–	–	–	7.8	–
Magnetite	–	–	–	6.5	–	–	–	–	–	–	–	–	–	–	–	–	–	–	–	–	–	–	–	–	–
Wüstite	–	–	–	1.1	–	–	–	–	–	–	–	–	–	–	–	–	–	–	–	–	–	–	–	–	–
Ilmenite	–	–	5.5	1.7	–	–	–	–	–	–	–	–	–	–	–	–	–	–	–	–	–	–	–	–	–
Anatase	0.7	1.1	–	–	–	1.0	–	–	–	–	–	–	–	–	–	–	–	–	1.9	–	–	–	–	–	–
Total (%)	*100.0*	*99.7*	*99.9*	*100.0*	*100.0*	*100.0*	*100.0*	*99.9*	*100.0*	*99.9*	*100.0*	*99.9*	*100.1*	*100.1*	*100*	*100*	*99.8*	*100.0*	*100.0*	*100.0*	*100.0*	*100.0*	*100.1*	*100.1*	*100.0*

Table 3
Major elements composition of studied samples. The data of the Petit Connétable samples (PC21-01 and 21-03) were also published in (Heller, 2022).

Element	SiO_2	Al_2O_3	Fe_2O_3	MnO	MgO	CaO	Na_2O	K_2O	TiO_2	P_2O_5	LOI	Total
1st camp.												
PC21-01	0.40	20.40	57.40	0.10	0.15	0.60	0.14	<L.D.	4.81	0.35	14.50	98.9
PC21-03	0.60	21.80	54.60	0.05	0.79	0.50	0.18	<L.D.	3.33	0.44	17.30	99.6
GC21-05	0.27	19.63	16.91	0.03	0.07	0.04	0.04	0.04	2.65	38.74	21.98	100.4
GC21-06	30.46	32.82	2.65	0.04	2.15	9.20	1.09	0.98	0.06	7.60	10.55	97.6
GC21-07	48.09	14.08	16.33	0.22	6.35	10.02	2.51	0.30	2.59	0.27	0.10	100.9
GC21-08	0.33	61.33	2.89	<L.D.	0.01	0.09	0.01	0.02	0.18	0.40	33.67	98.9
GC21-09	0.75	42.03	9.71	<L.D.	0.03	0.16	0.02	0.04	0.75	12.74	32.85	99.1
GC21-10	0.55	45.37	0.68	<L.D.	0.04	0.14	0.02	0.04	0.36	19.99	32.19	99.4
GC21-11	0.40	29.84	0.51	<L.D.	0.07	0.08	0.04	0.03	0.10	43.46	26.30	100.8
GC21-12	2.25	52.44	8.39	<L.D.	0.05	0.41	0.10	0.09	0.35	4.35	31.04	99.5
GC21-13	48.03	28.32	2.62	0.04	1.56	16.21	1.95	0.10	0.09	0.26	1.42	100.6
GC21-14	49.00	13.94	11.69	0.19	9.46	10.91	1.56	0.16	0.78	0.46	2.33	100.5
2nd camp.												
GC22-01	26.63	33.69	2.10	<L.D.	0.02	0.04	0.01	0.06	0.10	17.96	19.78	100.4
GC22-02	1.01	20.87	21.78	<L.D.	0.04	0.24	0.04	0.05	0.16	34.26	21.91	100.4
GC22-02B	1.10	24.88	9.20	<L.D.	0.02	0.23	0.01	0.04	0.24	40.08	24.10	99.9
GC22-03	3.23	27.09	1.23	<L.D.	0.13	0.49	0.39	0.14	0.36	40.67	26.35	100.1
GC22-04	36.50	33.39	1.51	0.01	0.21	1.40	0.79	0.22	0.06	0.82	24.65	99.6
GC22-06	0.42	17.96	28.50	<L.D.	0.03	0.07	0.01	0.05	0.38	32.25	19.99	99.7
GC22-07	0.64	60.61	3.55	<L.D.	<L.D.	0.00	<L.D.	0.01	0.43	1.27	32.97	99.5
GC22-08	0.27	22.28	12.77	0.02	0.01	0.09	0.02	0.17	1.92	40.80	22.60	101.0
GC22-09	<L.D.	47.82	2.10	<L.D.	<L.D.	0.06	<L.D.	0.02	0.49	16.00	32.09	98.6
GC22-10	<L.D.	55.20	3.60	<L.D.	0.00	0.33	0.01	0.09	0.35	3.53	35.89	99.0
GC22-10B	0.22	47.01	2.87	<L.D.	0.03	0.26	0.02	0.15	0.37	16.03	32.75	99.7
GC22-11	0.37	48.74	7.97	<L.D.	0.03	0.36	0.08	1.25	0.33	6.27	33.98	99.4
GC22-12	0.29	47.67	12.81	<L.D.	<L.D.	<L.D.	<L.D.	0.02	0.18	10.42	27.68	99.1
GC22-14	<L.D.	26.05	6.94	<L.D.	0.01	0.02	0.01	0.03	0.24	42.64	25.03	101.0

4.3. Major, trace and rare earth elements content

The main parent rock (B-GC21-13) has a high content of Si, Al, and Ca; as well as smaller amounts of Fe, Na and Mg, with respective oxide concentrations of 48, 28, 16, 3, 2, and 1.5 wt% (Table 3). These values are consistent with the mineralogical data presented in Fig. 5. High concentrations of Al and P are evident throughout the weathered profile, while Si is only present in high concentrations in kaolinite-rich samples at the base of the profile. The highest concentration of Fe is found in the duricrust. Al_2O_3 concentrations range from 20 to 60 wt%, P_2O_5 concentrations reach up to ~ 40 wt% in the matrix and up to ~ 45 wt% in fracture fillings, SiO_2 concentrations reach up to 35 wt%, and Fe_2O_3 concentration ranges from ~ 2 to ~ 60 wt% (highest in the duricrust of the Petit Connétable). Both the GC weathered profile and the PC duricrust are completely depleted of alkalis and alkali-earth elements (Table 3).

Trace element data are reported in Table 4 and Fig. 7 presents the rare earth element (REE) data of the bedrock and weathered rock, normalized to chondrite, for the GC and PC samples. Samples of the three bedrock lithologies exhibit flat REE patterns, indicating no significant fractionation between light REE (LREE: La to Nd) and heavy REE (HREE: Ho to Lu) (Fig. 7A). The anorthosite-like bedrock displays a positive anomaly in Eu, and lower normalized REE concentrations. Weathered rocks that have been formed over the anorthosite-like bedrock (regolith and the Fe-Al duricrust) generally show LREE enrichment compared to HREE. However, the only two kaolinite-rich samples GC22-1 and GC22-4, exhibit LREE depletion (Fig. 7B). Sample GC21-09 is notably more enriched in LREE, by a factor of up to 80, compared to the other GC regolith samples, which show enrichment factors of 2 to 10 relative to the anorthosite-like bedrock.

The REE patterns of the two samples formed over the Mesozoic dolerite dikes show a flat trend, with a Ce anomaly (Fig. 7C). These patterns differ markedly from those of samples formed over the Paleoproterozoic basement rocks (Fig. 7B). The REE patterns of the weathered rocks formed over an anorthosite-like protolith show a similar trend, but are less enriched than the Surinamese bauxite, as reported by Monsels and Van Bergen (2017, 2019) (Fig. 7B). The REE signature of the two duricrust samples from the PC resembles that of the GC regolith samples, but with less fractionation between LREE and HREE. The REE pattern of the PC duricrust also resembles that of the bauxitic-lateritic duricrust in the Kaw Mountains located at approximately 30 km from the Connétable Islands (Fig. 1) (Heller et al., 2022).

4.4. Petit Connétable (U-Th)/He geochronological data

A total of 31 (U-Th)/He ages were obtained from separated goethite and hematite sub-samples taken from two duricrust in PC. These ages range from 26.4 ± 2.6 Ma to 2.6 ± 0.4 Ma (Fig. 8 and Table 5), with U and Th concentrations ranging from 1 to 6 ppm and 1 to 19 ppm, respectively. Interestingly, the (U-Th)/He ages are similar in value and distribution to those obtained for the Kaw Mountain lateritic-bauxitic duricrust in French Guiana by Heller et al. (2022) (Fig. 8). Fig. 8B shows that the highest Th content is obtained for the youngest grains.

5. Discussion

5.1. Basement rock investigation

While all previous studies of Grand Connétable Island have identified the dominant Paleoproterozoic basement as a diorite, but petrological, geochemical and mineralogical data obtained in this study suggest the presence of an additional anorthosite-like protolith. Bulk mineralogy data show that this lithology, represented by sample B-GC-21-13, contains 62% plagioclase and 23% epidote (+ chlorite + vermiculite). Assuming that some of the epidote originated from the metamorphism/saussuritisation of plagioclase, this brings the total of primary plagioclase content is around 85%. This is higher than expected for a diorite, but within the range for an anorthosite (Best, 2003). This also explains the positive Eu anomaly (Fig. 7A), which is characteristic of rocks with a high plagioclase content, in which Eu^{2+} replaces Ca^{2+} in a reducing magma (Weill and Drake, 1973). Based on these results, and the presence of amphibolite, it can be proposed that the Paleoproterozoic GC basement contains a leucocratic part of a metamafic series, in addition to Mesozoic dolerite. To our knowledge, this is the first reported

Table 4
Rare earth elements and other trace elements composition of the studied samples (grouped by sampling campaign and location).

	Rare Earth Elements (μg/g)														Other trace concentrations (μg/g)										
	La	Ce	Pr	Nd	Sm	Eu	Gd	Tb	Dy	Ho	Er	Tm	Yb	Lu	Cu	Zn	Rb	Sr	Y	Zr	Cs	Ba	Hf	Th	U
1st camp. (PC)																									
PC21-01	3.05	5.05	0.643	2.260	0.444	0.127	0.350	0.058	0.393	0.082	0.242	0.039	0.301	0.047	192.0	39.6	0.0	347.0	1.84	63.90	0.00	0.00	6.80	1.73	4.10
PC21-03	12.40	20.30	2.130	6.340	0.989	0.217	0.646	0.101	0.640	0.139	0.434	0.069	0.547	0.086	106.0	35.1	190.0	73.3	3.69	178.00	0.00	0.00	9.40	4.69	9.60
1st camp. (GC)																									
GC21-05	1.59	9.18	0.490	2.370	0.760	0.240	0.830	0.150	0.930	0.170	0.500	0.070	0.500	0.070	119.4	130.7	0.17	5.98	2.71	40.48	0.00	47.90	0.73	0.53	1.17
GC21-06	0.537	1.20	0.156	0.658	0.173	0.253	0.230	0.039	0.256	0.054	0.170	0.027	0.158	0.027	48.5	46.3	2.67	169.0	1.33	1.74	0.09	21.10	0.05	0.04	0.05
GC21-07	10.67	27.86	4.160	20.460	5.940	2.090	6.680	1.110	6.700	1.300	3.550	0.490	3.050	0.450	336.4	112.5	5.45	209.1	33.11	161.17	0.26	78.35	4.49	0.27	0.94
GC21-09	17.50	26.03	3.470	10.370	1.520	0.280	1.070	0.130	0.570	0.090	0.270	0.040	0.220	0.030	4.8	23.0	0.55	23.8	1.82	202.40	0.08	9.63	4.75	2.13	13.79
GC21-11	1.01	2.73	0.180	0.580	0.100	0.020	0.100	0.010	0.090	0.020	0.040	0.010	0.040	0.010	15.9	329.9	0.07	1.7	0.22	24.49	0.00	1.06	0.75	0.99	3.94
GC21-10	2.57	4.28	0.460	1.550	0.220	0.050	0.210	0.020	0.120	0.020	0.060	0.010	0.060	0.010	11.5	144.3	0.12	6.5	0.41	50.24	0.00	8.79	1.15	0.57	2.10
GC21-08	0.65	1.96	0.120	0.390	0.050	0.010	0.050	0.000	0.030	0.010	0.010	0.000	0.010	0.000	1.6	1.39	0.03	11.8	0.11	22.95	0.00	0.85	0.70	0.22	1.39
GC21-12	0.84	2.81	0.240	0.920	0.180	0.050	0.150	0.020	0.080	0.010	0.040	0.010	0.050	0.000	28.2	30.8	1.12	4.97	0.21	31.59	0.03	15.36	0.92	0.35	1.10
GC21-13	0.81	1.97	0.260	1.160	0.340	0.280	0.470	0.090	0.580	0.130	0.380	0.050	0.330	0.050	14.2	14.7	2.23	202.0	3.10	8.20	0.10	28.30	0.23	0.36	0.16
GC21-14	4.79	12.05	1.780	8.390	2.190	0.800	2.590	0.440	2.690	0.580	1.660	0.240	1.530	0.240	2.4	73.4	1.37	122.2	14.14	45.27	0.10	30.18	1.33	0.26	0.69
2nd camp. (GC)																									
GC22-01	0.030	0.23	0.040	0.270	0.110	0.040	0.130	0.020	0.190	0.040	0.120	0.020	0.110	0.010	17.0	120.0	0.61	7.6	1.10	1.40	0.09	6.50	0.04	0.09	0.13
GC22-02	1.30	2.60	0.260	0.840	0.150	0.040	0.090	0.020	0.110	0.020	0.050	0.010	0.060	0.010	24.0	130.0	0.34	11.0	0.45	16.00	0.02	3.60	0.43	1.50	0.35
GC22-02B	2.30	4.50	0.470	1.600	0.280	0.060	0.210	0.030	0.160	0.030	0.080	0.010	0.100	0.020	60.0	270.0	0.47	23.0	0.69	15.00	0.03	12.00	0.37	1.90	0.68
GC22-03	4.80	9.10	0.970	3.100	0.550	0.100	0.440	0.060	0.390	0.070	0.200	0.030	0.230	0.040	33.0	390.0	0.57	24.0	2.00	35.00	0.02	9.80	0.90	3.20	1.50
GC22-04	0.09	0.53	0.100	0.530	0.170	0.070	0.190	0.030	0.220	0.050	0.120	0.020	0.080	0.010	15.0	32.0	1.80	44.0	1.00	2.20	0.26	5.70	0.07	0.05	0.11
GC22-06	6.00	12.00	1.200	4.000	0.660	0.120	0.470	0.070	0.380	0.070	0.200	0.030	0.230	0.050	16.0	140.0	0.18	17.0	1.70	64.00	0.01	7.00	1.70	11.00	0.96
GC22-07	4.70	8.50	0.840	2.500	0.350	0.070	0.250	0.040	0.200	0.040	0.130	0.020	0.160	0.030	12.0	4.9	0.01	11.0	1.00	53.00	0.00	4.10	1.40	4.80	0.45
GC22-08	1.20	4.90	0.350	1.500	0.390	0.110	0.410	0.070	0.430	0.090	0.270	0.050	0.350	0.050	110.0	94.0	0.64	5.8	1.70	23.00	0.01	4.00	0.50	0.74	0.33
GC22-09	5.10	11.00	1.100	3.300	0.560	0.100	0.370	0.050	0.300	0.050	0.160	0.020	0.170	0.030	13.0	52.0	0.11	15.0	1.20	99.00	0.02	17.00	2.30	11.00	0.92
GC22-10	2.50	4.20	0.450	1.300	0.230	0.040	0.140	0.020	0.120	0.020	0.080	0.010	0.080	0.020	12.0	4.40	0.04	39.0	0.61	43.00	0.00	5.80	1.00	3.00	0.39
GC22-10B	1.60	2.80	0.320	1.100	0.190	0.040	0.090	0.010	0.100	0.020	0.050	0.010	0.060	0.010	22.0	130.0	0.67	24.0	0.46	38.00	0.01	30.00	0.83	1.90	0.40
GC22-11	1.60	2.60	0.250	0.880	0.110	0.030	0.100	0.010	0.060	0.020	0.040	0.010	0.040	0.010	12.0	120.0	0.72	98.0	0.37	43.00	0.00	51.00	0.96	1.00	0.35
GC22-12	0.22	0.59	0.060	0.200	0.040	0.020	0.030	0.010	0.040	0.010	0.020	0.000	0.020	0.000	76.0	15.0	0.05	3.70	0.13	9.50	0.01	21.00	0.23	0.40	0.24
GC22-14	3.60	7.60	0.770	2.500	0.410	0.090	0.330	0.040	0.200	0.040	0.100	0.020	0.110	0.020	20.0	270.0	0.09	8.10	0.94	41.00	0.00	4.50	0.89	5.30	0.66

Table 5
Goethite/hematite (U-Th)/He data.

Sub sample	aliquot	weight	^{4}He	^{4}He error	^{4}He	^{238}U	^{232}Th	^{147}Sm	^{238}U	^{232}Th	^{147}Sm	Th/U	raw age	corrected age	σ age	diff. corr. factor[1]	predominant
		(μg)	(mol)	(mol)	(mol/g)	(ng)	(ng)	(ng)	(ppm)	(ppm)	(ppm)		(Ma)	(Ma)	(Ma)	(%)	(mineral)[$]
PC21-01_A	PC01A1	17	1.92E-15	3.39E-16	1.13E-10	0.01	0.06	0.00	0.38	3.57	0.05	9.4	16.9	17.7	3.7	5	Hm
PC21-01_A	PC01A2	28	1.56E-15	1.78E-16	5.58E-11	0.02	0.04	0.00	0.66	1.55	0.09	2.4	10.2	10.7	1.7	5	Hm
PC21-01_A	PC01A3	52	8.03E-16	1.83E-16	1.54E-11	0.03	0.08	0.00	0.50	1.56	0.08	3.1	3.2	3.4	1.1	5	Hm
PC21-01_A	PC01A4	127	9.37E-15	2.05E-16	7.38E-11	0.04	0.33	0.01	0.35	2.56	0.04	7.4	14.3	15.0	1.5	5	Hm
PC21-01_A	PC01A5	56	7.58E-16	2.14E-16	1.35E-11	0.02	0.10	0.00	0.31	1.77	0.02	5.7	3.5	3.7	1.3	5	Hm
PC21-01_B	PC01B1	125	1.12E-14	4.46E-16	8.92E-11	0.62	0.47	0.01	4.97	3.74	0.07	0.8	2.8	2.9	0.3	5	Hm
PC21-01_B	PC01B2	42	2.28E-15	3.57E-16	5.42E-11	0.02	0.14	0.00	0.56	3.31	0.04	5.9	7.4	7.8	1.5	5	Hm
PC21-01_B	PC01B3	59	8.48E-15	2.14E-16	1.44E-10	0.17	0.27	0.02	2.96	4.60	0.31	1.6	6.6	6.9	0.7	5	Hm
PC21-01_B	PC01B4	98	1.12E-14	4.10E-16	1.14E-10	0.04	0.30	0.00	0.38	3.05	0.04	8.0	19.4	20.4	2.0	5	Hm
PC21-01_B	PC01B5	103	9.82E-15	4.28E-16	9.53E-11	0.25	0.43	0.00	2.46	4.13	0.04	1.7	5.2	5.5	0.5	5	Hm
PC21-01_C	PC01C1	83	8.48E-15	4.19E-16	1.02E-10	0.04	0.28	0.01	0.52	3.38	0.07	6.5	14.3	15.0	1.5	5	Hm
PC21-01_C	PC01C2	115	1.25E-14	4.42E-16	1.09E-10	0.04	0.21	0.00	0.36	1.85	0.04	5.2	25.1	26.4	2.6	5	Hm
PC21-01_C	PC01C4	67	7.14E-15	3.61E-16	1.07E-10	0.03	0.35	0.01	0.47	5.27	0.09	11.2	11.3	11.9	1.2	5	Hm
PC21-01_C	PC01C5	101	1.67E-14	3.86E-16	1.65E-10	0.03	0.78	0.01	0.34	7.74	0.08	22.4	14.1	14.8	1.5	5	Hm
PC21-01_D	PC01D1	101	1.64E-14	4.52E-16	1.63E-10	0.16	0.95	0.01	1.55	9.44	0.10	6.1	8.0	8.4	0.8	5	Hm
PC21-01_D	PC01D2	234	3.68E-14	4.35E-16	1.57E-10	0.18	2.99	0.02	0.77	12.78	0.07	16.6	7.7	8.1	0.8	5	Hm
PC21-01_D	PC01D3	172	1.38E-14	4.16E-16	8.03E-11	0.05	0.94	0.01	0.29	5.45	0.04	18.8	9.4	9.9	1.0	5	Hm
PC21-03_A	PC03A1	38	5.06E-15	3.76E-16	1.33E-10	0.09	0.27	0.01	2.49	7.12	0.23	2.9	5.9	6.5	0.6	10 ± 10	Hm-Goe
PC21-03_A	PC03A2	48	1.04E-14	4.18E-16	2.17E-10	0.12	0.35	0.01	2.48	7.25	0.26	2.9	9.6	10.5	1.0	10 ± 10	Hm-Goe
PC21-03_A	PC03A3	80	1.33E-14	4.98E-16	1.66E-10	0.16	0.45	0.01	1.97	5.62	0.16	2.9	9.3	10.3	1.0	10 ± 10	Hm-Goe
PC21-03_A	PC03A4	73	4.14E-15	4.63E-16	5.67E-11	0.17	0.54	0.02	2.39	7.40	0.24	3.1	2.5	2.8	0.4	10 ± 10	Hm-Goe
PC21-03_A	PC03A5	100	1.60E-14	4.64E-16	1.60E-10	0.26	0.71	0.02	2.59	7.14	0.25	2.8	7.0	7.6	0.7	10 ± 10	Hm-Goe
PC21-03_B	PC03B1	32	7.28E-16	1.94E-16	2.28E-11	0.02	0.07	0.00	0.77	2.15	0.00	2.8	3.3	3.6	1.3	10 ± 10	Hm-Goe
PC21-03_B	PC03B2	16	7.19E-16	2.17E-16	4.49E-11	0.02	0.07	0.00	1.40	4.37	0.04	3.1	3.4	3.8	1.3	10 ± 10	Hm-Goe
PC21-03_B	PC03B3	29	1.20E-15	2.15E-16	4.13E-11	0.02	0.07	0.00	0.68	2.38	0.02	3.5	6.2	6.8	1.4	10 ± 10	Hm-Goe
PC21-03_B	PC03B4	40	1.46E-15	2.24E-16	3.66E-11	0.03	0.11	0.00	0.85	2.80	0.09	3.3	4.5	4.9	0.9	10 ± 10	Hm-Goe
PC21-03_B	PC03B5	67	1.50E-15	2.61E-16	2.24E-11	0.03	0.12	0.00	0.43	1.77	0.00	4.1	4.9	5.4	1.1	10 ± 10	Hm-Goe
PC21-03_C	PC03C2	19	3.20E-15	3.81E-16	1.69E-10	0.07	0.26	0.01	3.92	13.81	0.33	3.5	4.4	4.8	0.7	10 ± 10	Hm-Goe
PC21-03_C	PC03C3	40	3.51E-15	2.08E-16	8.77E-11	0.11	0.36	0.01	2.66	8.99	0.21	3.4	3.4	3.7	0.4	10 ± 10	Hm-Goe
PC21-03_C	PC03C4	31	1.47E-14	2.32E-16	4.76E-10	0.18	0.58	0.03	5.90	18.77	0.89	3.2	8.5	9.4	0.9	10 ± 10	Hm-Goe
PC21-03_C	PC03C5	101	8.93E-15	2.47E-16	8.85E-11	0.17	0.79	0.02	1.70	7.80	0.21	4.6	4.6	5.1	0.5	10 ± 10	Hm-Goe

1- He diffusional loss correction factor with error.
$: Hm: hematite: Goe: goethite.

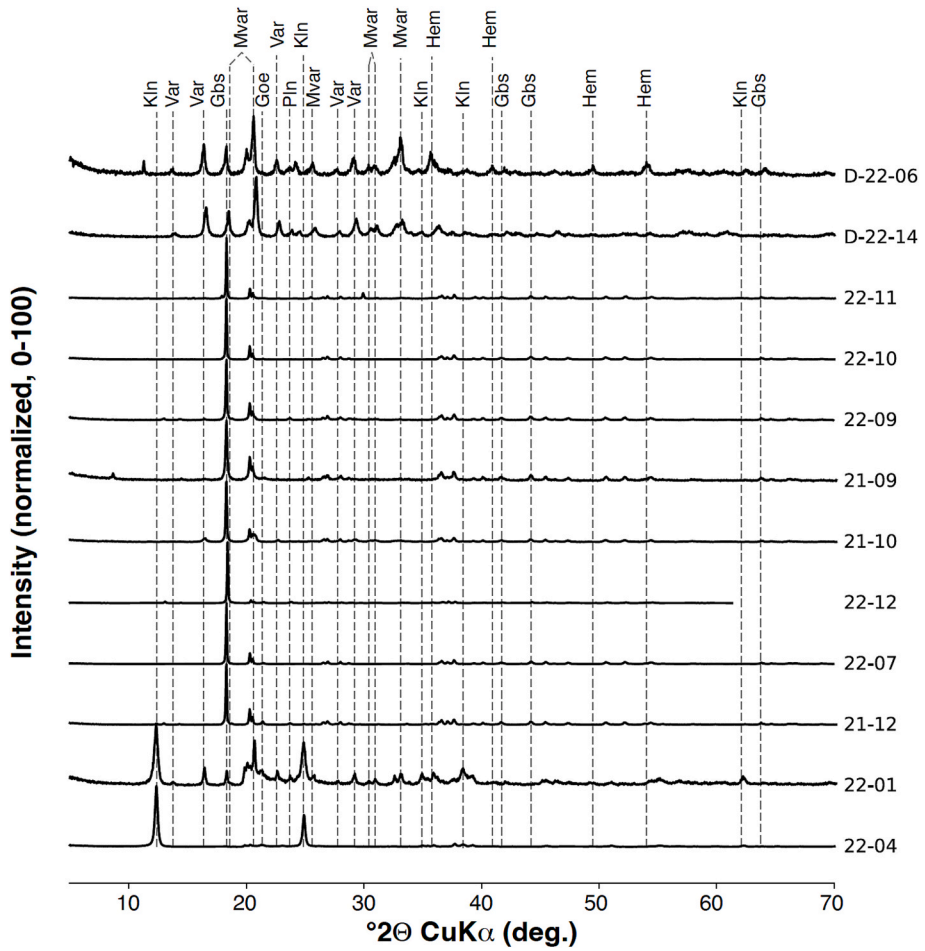

Fig. 4. The major mineral phases of the Grand Connétable regolith are displayed in the X-ray diffractograms of the analysed bulk samples. The intensities were normalized using the min–max normalization method (Han et al., 2011). Sample locations are arranged from bottom to top in ascending order of elevation.

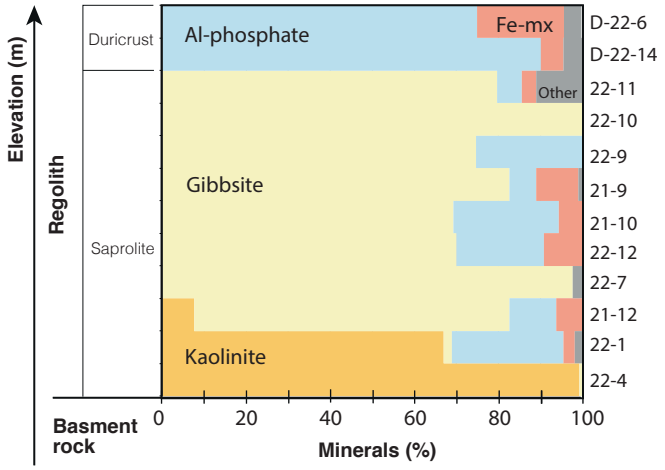

Fig. 5. The XRD-determined bulk mineralogy of the samples studied along the regolith profile is reported, excluding the vein samples and the dolerite-developed regolith samples. As several samples were collected from around the same elevation, it is not possible to provide more precise elevation values. The samples are arranged from top to bottom in order of decreasing altitude. (Fe-mx represents Fe-minerals: hematite + goethite, and Al phosphates: (meta) variscite + planerite). In addition, the P-Al-Fe duricrust samples, collected from lower in the profile, are positioned at the top based on geological logic.

occurrence of anorthosite-type lithology reported in the northern part of French Guiana. However, anorthosite lithology is however consistent with the filiation hypothesized by Cautru et al. (1998) for the gabbro-dioritic "Mahury Complex" (2,144 ± 2 Ma at the Mahury Mount), which is located south of Cayenne (Delor et al., 2003). An anorthosite has also been described in the Paleoproterozoic granulite belt of the Guiana Shield (Kroonenberg et al., 2019).

5.2. *Weathering and chemical transfer*

The variation in the concentrations of major elements, REE and other trace elements across samples representing different levels of the Grand Connétable profile reflects its weathering regime and the addition of elements from other sources such as bird guano and seawater. Regarding the GC regolith samples, we consider the anorthosite-like composition of the fresh sample B-GC-21-13 to be representative of the underlying basement rock, although further bedrock sampling is required to determine its precise composition more accurately. The parent rock-normalized major element concentrations of the regolith (Fig. 9), along with the mineralogical composition data, show that the regolith is enriched in Ti, Fe, K and P. The enrichment of Ti and Fe in the regolith is well-known to be associated with the bedrock weathering and the precipitation of ilmenite or anatase, and iron oxyhydroxide respectively (Tardy, 1992). However, the elevated K and P content is elevated in the regolith is sourced from guano transformed into phosphoric acid (formed by mineralization of the guano with rainwater and microbial activity), which contains significantly higher concentrations of K and P than the anorthosite-like bedrock (Fig. 9A). In contrast, normalization to the guano-rich sample (Fig. 9B) suggests that all bedrock lithologies

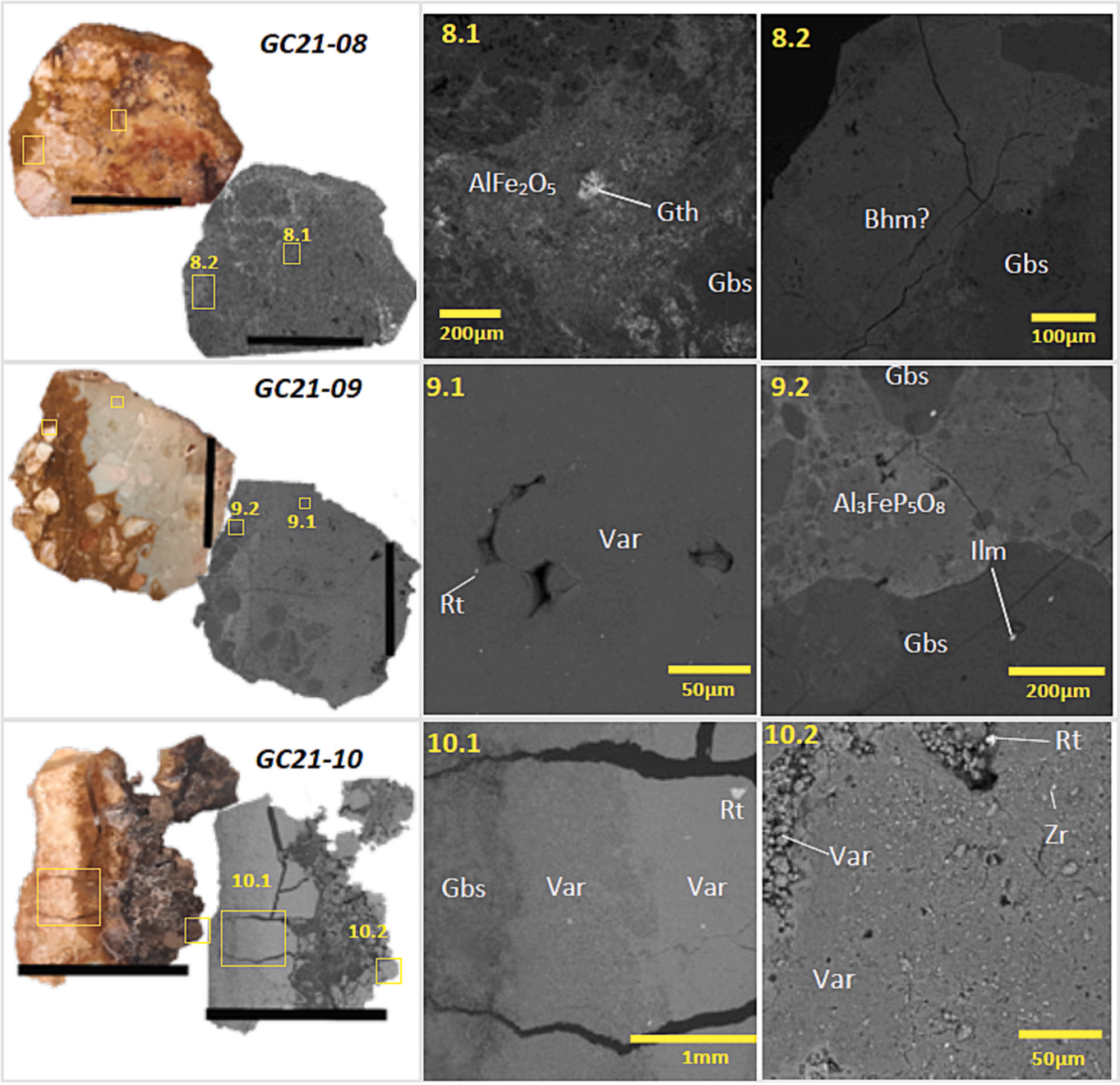

Fig. 6. The mineralogy of some of the GC regolith samples was determined using BSE. The scale bars on the studs and micrographs in the left-column are 10 mm long. Mineral name abbreviations are taken from (Warr, 2021): Var: variscite or metavariscite, Ilm: ilmenite, Gth: goethite, Bhm: boehmite Rt: rutile / anatase, Zr: zircon.

naturally contain higher concentrations of LREEs and insoluble trace elements (U, Th, Hf) than the guano. This suggests that the elevated concentrations of these elements in the regolith are primarily due to the weathering of the bedrock, rather than external input from the guano. However, the latter's contribution cannot be entirely ruled out. In contrast, elements such as Cu and Zn which can even be leached away depending on the weathering environment; may have a higher guano-derived fraction in the regolith, as they are more concentrated in the guano than in the anorthosite-like bedrock. Finally, traces of sulphate (SO_4) combined with Ca, Al and K detected at very small scales by SEM-BSE analysis and by XRD (calcium alumino-sulfate ($Ca_4Al_6O_{12}SO_4$) and alunite ($KAl_3(SO_4)_2(OH)_6$)) (Fig. 6 and S4). These can be attributed to the contribution of sea spray.

The REE signatures of the regolith samples (excluding the dolerite-derived samples), normalized to the parent rock (Fig. 10A), show that all samples are depleted in HREE and most are depleted in MREE. This indicates that weathering at GC leached both HREE and MREE. Conversely, most of the samples show enrichment in LREE compared to the initial parent rock. Two kaolinite-rich samples (GC22-01 and 04) display unique REE patterns as shown in Fig. 7. The LREE-depleted and least enriched samples exhibit a positive Ce anomaly (Fig. 8A), which suggests that trivalent LREE are more mobile than the tetravalent Ce (IV). The reversal of the Eu anomaly from positive in the anorthosite-like parent rock (Fig. 7A) to negative in the anorthosite-derived bauxite (Fig. 7 and 10A) indicates initial Eu enrichment by the fractionation of Eu^{2+} in plagioclase, followed by depletion through plagioclase weathering. Overall, the LREE/HREE fractionation in relation to the initial anorthosite bedrock indicates that LREE are less soluble than Eu and

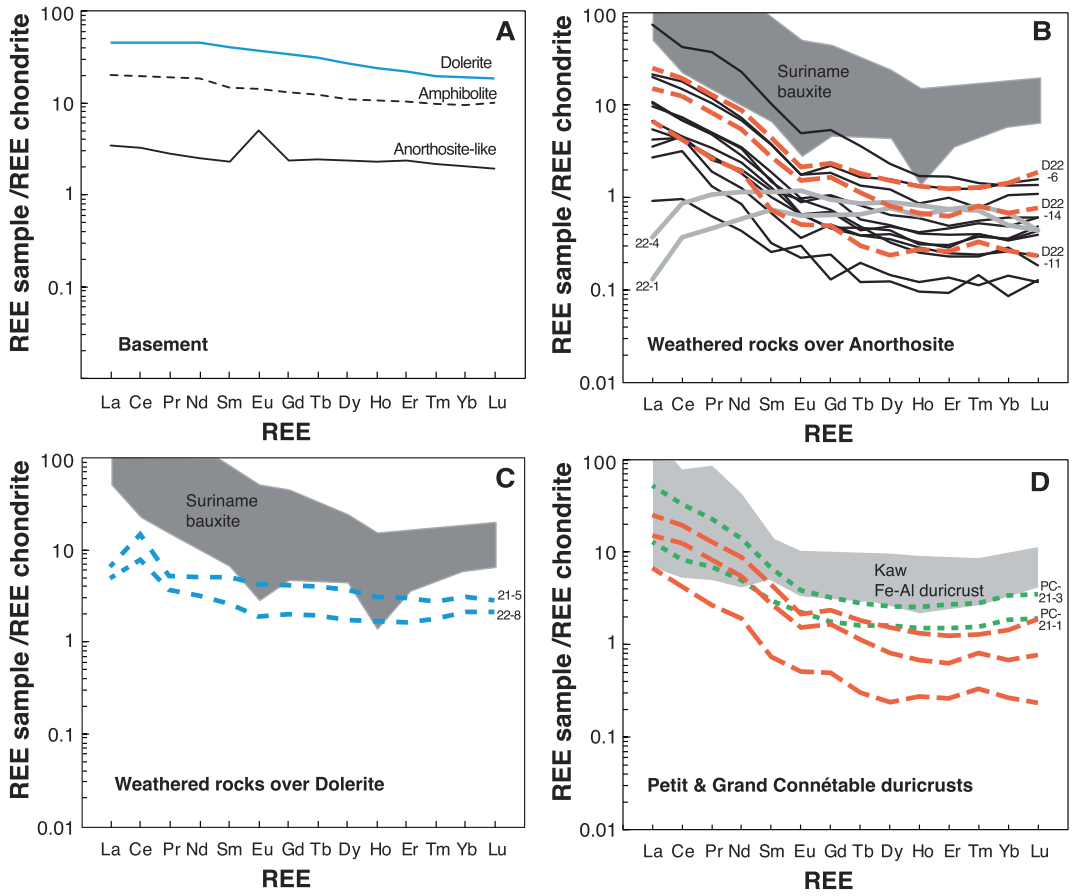

Fig. 7. Chondrite normalized REE concentrations pattern of the Grand and Petit Connétable Islands samples (Chondrite REE from McDonough and Sun (1995)). (A) Bedrock samples (anorthosite, amphibolite and dolerite). (B) Weathered rocks over anorthosite, showing colour differentiation between the regolith samples (black and grey) and Fe-duricrust (red dotted lines). (C) Weathered rocks over dolerite (blue). The dark grey fields on Figures B and C represent the REE pattern obtained for Surinamese bauxite samples (Monsels and Van Bergen, 2017; 2019). (D) Petit Connétable duricrust samples (green thin dotted lines), with the Grand Connétable samples of Fig. 7B superimposed for comparison (red dotted lines). The light grey shape represents the REE pattern obtained for the Kaw bauxitic-lateritic duricrust samples (Heller et al., 2022).

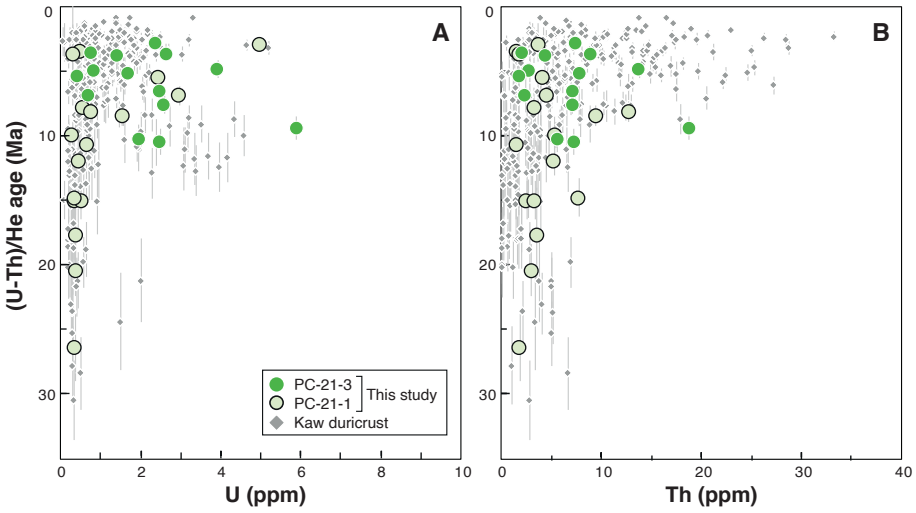

Fig. 8. Petit Connétable hematite and goethite (U-Th)/He ages has a function of (A) the U and (B) the Th concentration (light and dark green circles). For comparison, data of the Kaw Mountain lateritic duricrust from Heller et al. (2022) are presented in grey (diamonds).

HREE in the physicochemical conditions that enhanced weathering at GC. This positive correlation between the degree of fractionation and the extent of weathering is characteristic of lateritic and bauxitic weathering, as by Berger et al. (2014) have previously suggested. Interestingly, the REE patterns of weathered rocks that developed on anorthosite-rich protolith of GC and PC duricrusts have the same trend as those of Suriname bauxites and Kaw laterite/bauxite (Heller et al., 2022; Monsels and Van Bergen, 2017; 2019), as illustrated in Fig. 7. However, REEs are

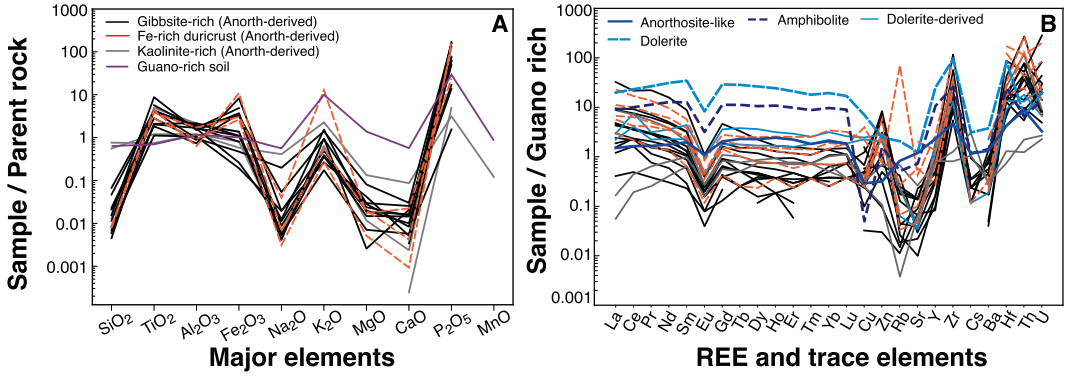

Fig. 9. (A) Normalization of the concentrations of major elements in the regolith relative to the main bedrock (anorthosite-like) reveals an enrichment in insoluble elements such as Al, Fe, and Ti, alongside a depletion of more soluble elements, including alkali metals, alkaline earth metals, and Mn. The comparatively smaller depletion of K, relative to Na, Ca, and Mg, as well as elevated P concentrations, may be attributed to the influence of guano, which is richer in K and P than the bedrock. (B) Normalization of REE and trace element concentrations in the guano-rich sample (GC21-06).

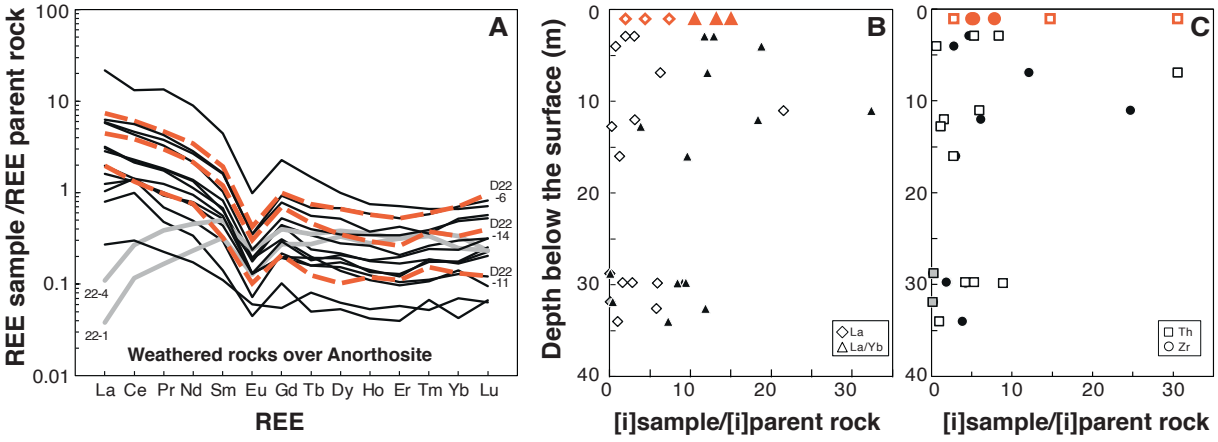

Fig. 10. The evolution of REE and some trace element concentrations is shown normalized to the parent rock. Only the weathered samples (bauxite and duricrust) developed on the anorthosite are reported. (A) REE pattern. (B) Evolution of the La concentration and La/Yb ratio as a function of the depth below the surface and (C) evolution of the Th and Zr concentrations as a function of the depth below the surface. Error bars are within the symbols. As the Grand Connétable was reworked during P exploitation, we assumed the original top elevation to be 2 m higher than it is now. As in Fig. 7, the grey and red symbols represent the GC22-1&4 and the duricrust samples, respectively.

less enriched at GC, which may be explained by the volume dilution associated with the formation of P-Al-rich minerals, although different REE concentrations in the respective protoliths cannot be ruled out. Indeed, most GC island samples contain 10–80% P-Al minerals, as illustrated in Fig. 5. This is clearer when comparing Fe-Al and Fe-Al-P duricrust samples from PC and GC respectively, where the lower rare earth elements concentration in GC Fe-Al-P duricrust samples is evident (Fig. 7D). Furthermore, saprolite samples that mainly contain kaolinite (22-1 and 22-4) exhibit a distinct REE pattern. This suggests that REE enrichment is influenced by the presence of gibbsite and iron-rich minerals such as hematite and goethite, as well as the volume dilution associated with Fe-Al phosphate and Ca-K sulfate minerals.

In addition, Fig. 10B and C show how the La concentration, the La/Yb ratio and the Th and U concentrations change with depth below the surface of the GC bauxite and the Fe-Al duricrust. As we were unable to determine the sample density due to the secondary addition of phosphate and sulfate affecting the entire system, we are simply presenting the evolution of these with depth rather than using the transport function (τ) obtained by mass-balance calculations. While there is no visible relationship between La concentration and depth, the La/Yb ratio, which acts as a proxy for the LREE/HREE evolution, shows a slight negative correlation with depth. Samples taken from 2 to 15 m depth below the top surface of the GC present a higher La/Yb ratio than those taken from deeper depth (28–35 m below the surface). This indicates that LREE and HREE are more fractionated in the upper, most weathered part of the profile. A similar trend is observed with immobile elements such as Zr and Th, which are also more enriched in the upper part of the regolith (Fig. 10C). However, the extensive enrichment of phosphorus from the guano and its subsequent transformation into phosphoric acid could have induced additional chemical transfers, in addition to previous lateritic and bauxitic weathering. This complicates the interpretation of the regolith's formation compared to that of a classical lateritic-bauxitic regolith.

5.3. *Mechanism of phosphate and sulphate minerals formation*

The enrichment in phosphorous reflects the formation of heterogeneously distributed alumino-phosphate minerals following a reaction between guano-derived phosphoric acid and gibbsite, as well as iron oxyhydroxide to a lesser extent. The Al-phosphate minerals variscite, metavariscite and planerite were observed in the GC regolith samples. Mineralogical studies have shown that variscite ($AlPO_4{\cdot}2H_2O$) is the phosphorous endmember of an isostructural series of dihydrates phosphates, in which strengite ($FePO_4{\cdot}2H_2O$) is the iron endmember. These endmembers have an orthorhombic structure in structure, and their respective polymorphic counterparts, metavariscite and metastrengite, have a monoclinic structure (Kiratisin and Demaille, 2006). There are also total solid solution series between variscite and strengite, in which

some of the Al is substituted by Fe to form as phase referred by the authors as ferric variscite (Kiratisin and Demaille, 2006). Additionally, heterosite ($Fe^{3+}(PO_4)$) has been identified by XDR in one sample (Table 2), demonstrating the presence of a wide variety of phosphate minerals. However, the existence of solid solution series in this system can explain phases that are sometimes observed on the BSE (e.g., in sample GC21-09). As described by Lindsay et al. (1989) and Dill (2000), variscite can be either hypogene or supergene in origin. In both cases Al comes from the host alumino-silicate rocks and P can be brought from magmatic or submarine hydrothermal activities in the first case, or from biogenic deposits in the second. The parent rocks of the GC have a very low phosphorous content (0.2–0.3% P_2O_5), and submarine hydrothermal circulation is not an option, as the laterization and bauxitization processes attest to an emerged continental environment. Furthermore, no other phosphate deposits are known in the region around French Guiana or on the Guiana Shield. Therefore, as Dill (2000) explains, it is certain that the phosphorous contributing to the formation of phosphate minerals results from the interaction of infiltrated phosphoric acid originating from guano and gibbsite, following the reaction in equation 1:

$$A(OH)_3 + HPO_4^{2-} + 2H^+ \rightarrow Al(PO_4).2H_2O + H_2O \quad (1)$$

Foord and Taggart (1986) added planerite, with empirical formula $(Cu_{0.23}(H_2)_{0.77})_{1.00}Al_{5.97}(PO_4)_{4.00}(OH)_{7.91}\cdot 4H_2O$ to the turquoise group of minerals. This mineral was detected in five studied samples (GC21-12, GC22-8, 9, 10B and 12), but the affinity with Cu and Zn observed in previous studies (Matsubara and Kato, 1994) was not evident here. No correlation was found between the content of either Cu or Zn and the presence of planerite (Tables 2 and 3), demonstrating that these elements do not determine the presence of this mineral. Additionally, Ti-phosphate minerals have been identified at levels of 0.8–1.5%, with the highest concentrations of Al-phosphate minerals found (Table 2). No titanium-rich minerals (such as anatase or ilmenite) have been detected by XRD as it is often observed up to 2–3 wt% (e.g. Heller et al., 2022), and only micrometric Ti-rich minerals have been observed on the BSE images (Fig. 6). This suggests that phosphoric acid interacts strongly with all the mineral phases present in the regolith, resulting in the precipitation of new phosphate-rich minerals containing Al, Fe and Ti.

Several samples (GC22-02B, 22-03, 33-06, and 22-14) contain 3–4% of calcium alumino-sulfate ($Ca_4Al_6O_{12}SO_4$), whereas one sample (GC22-11) contains 11% of alunite ($KAl_3(SO_4)_2(OH)_6$), as detected by XRD (Table 1). A $CaSO_2$ phase was also observed to a lesser extent in GC21-12 during BSE analysis (Fig. S4). Interestingly, no calcium sulphate phases were detected in the two PC duricrust samples, which calls into question the origin of the sulphur and calcium in the GC. These elements likely originated from an external source, since Ca is normally leached by weathering during the formation of the laterite, and S is not present in the parent rock. Ocean water is a likely source of Ca, K and SO_4, and birds' guano is an obvious source of post-weathering input of Ca, as it contains ~10% Ca (sample GC21-06; Table 2). XRD data show that the calcium alumino-sulfate and alunite phases occur alongside elevated (75–90%) amounts of Al-phosphate minerals, variscite and metavariscite. SEM-BSE petrographs show that the $CaSO_2$ phase occurs alongside planerite (Fig. S4). Taken together, these factors suggest the necessity of the co-occurrence and co-percolation of Ca-rich guano and $CaSO_4^-$ bearing ocean water (probably in the form of sea spray) for the formation of the observed sulphate phases in the regolith.

5.4. Implication for the lateritic to bauxitic formation

The mineralogy of the GC and PC samples reveals the presence of mostly gibbsite, and in some cases, kaolinite. The dominance of gibbsite suggests that the regolith is bauxite. Although we have no information on the continuation of the Petit Connétable profile underwater, the presence of gibbsite in the Fe-Al duricrust indicates a bauxitic signature. A similar result was obtained in the Fe-Al duricrust of the Kaw mountains (Fig. 1B), as proposed by Heller et al. (2022).

In addition, the hematite and goethite (U-Th)/He geochronological results obtained from PC samples reveal the formation of laterite to bauxite over geological time. The ages indicate that the onset of lateritization began at ~30 Ma. The oldest ages, from ~30 to >10 Ma, exhibit lower U and Th concentrations (Fig. 8), with a predominance of hematite. Aliquots younger than 10 Ma, up to 3 Ma, including all PC-21-3 data and some PC-21-1 data, which are richer in goethite, are characterized by higher U and Th concentration (Fig. 8). The progressive Th enrichment is similar to that observed in Kaw Mountain samples by Heller et al. (2022) (Fig. 1A and B). Based on mineralogical and geochemical changes, notably Th enrichment and Al substitution in goethite, the authors, of that study concluded that weathering started during the Oligocene with ferruginous laterite formation, and that during the late Neogene, the climate shifted to more humid conditions. This led to the partial transformation of the ferruginous laterite into bauxite. Based on the presence of Fe-Al duricrusts in Grand and Petit Connétable, and the (U-Th)/He data obtained in the Petit Connétable, we propose that both islands share similar weathering conditions to those of Kaw Mountains. This would involve an initial laterization episode in the Oligocene, during which both kaolinite and iron oxy-hydroxides would be formed (these are typical of lateritic profiles), followed by a second weathering event at the end of the Miocene associated with bauxitization. Remarkably, the weathering at Grand Connétable is more advanced, with the bauxitic part of the weathered profile much thicker (30 of 35 m, after exploitation are composed of gibbsite), than in other places in the region such, as at Kaw Mountains (5 m of 72 m composed of gibbsite; Heller et al., 2022), and Surinamese bauxites (10 m deep; Monsels and Van Bergen, 2017; 2019). One reason for this difference in weathering products could be the difference in the bedrock; while the regolith at Grand Connétable is silica poor anorthosite-like, the regolith at Kaw Mountain is developed on acid-to-intermediate metavolcanic rocks (Delor et al, 2003). Another possible explanation is the different paleodrainage conditions associated with the low elevation, where the drainage conditions could have facilitated bauxite weathering. As bauxites often occur often in proximity to the sea (Bardossy and Aleva, 1990), the proximity of Grand Connétable to the sea might contribute to the occurrence of its thick bauxitic profile. Reasons for this difference could include chemically different rainwater composition and direct deposition of sea spray.

Finally, the obtained (U-Th)/He ages of the Connétable Islands call into question the geomorphological model proposing the development of paleosurfaces over the Guiana craton. Several authors have suggested that the Guiana shield has 4–5 planation surfaces with different ages ranging from the late Cretaceous to the Quaternary (Choubert, 1957; King, 1962; McConnell, 1968; Blancaneaux, 1981; Aleva, 1984; Bardossy and Aleva, 1990). These models were established mainly for the central areas of the shield. It has been suggested that the ages of laterite and bauxite are dependent on elevation, with ages ranging from the Oligocene-Lower Miocene (>300 m a.s.l.) to the Quaternary (<150 m a.s.l.) having been identified in French Guiana (Blancaneaux, 1981; Choubert, 1957; Sapin et al., 2016). Fig. 11A presents the geomorphological model of the Guiana shield from McConnell (1968) and Blancaneaux (1981) with the planation surfaces proposed for the Guianas. Whereas Fig. 11B presents the obtained hematite and goethite (U-Th)/He ages including those from Heller et al. (2022) and for the Connétable site along a southwest-northeast transect. Interestingly, there are no significant age differences between the Kaw Mountains and the Connétable Islands, despite the site's elevation (Fig. 11B). The top of Kaw Mountain is suggested to belong to "Surface II" according to Blancaneaux (1981) and Choubert (1957) (marked in blue on Fig. 11A). While the model makes sense for Kaw Mountain this is not the case for the Connétable Islands. Red ellipse shows how the new ages obtained for Connétable (Fig. 11A) could fit into the proposed model corresponding to "Surface II" as the Kaw Mountain. The Fig. 11 shows that the too

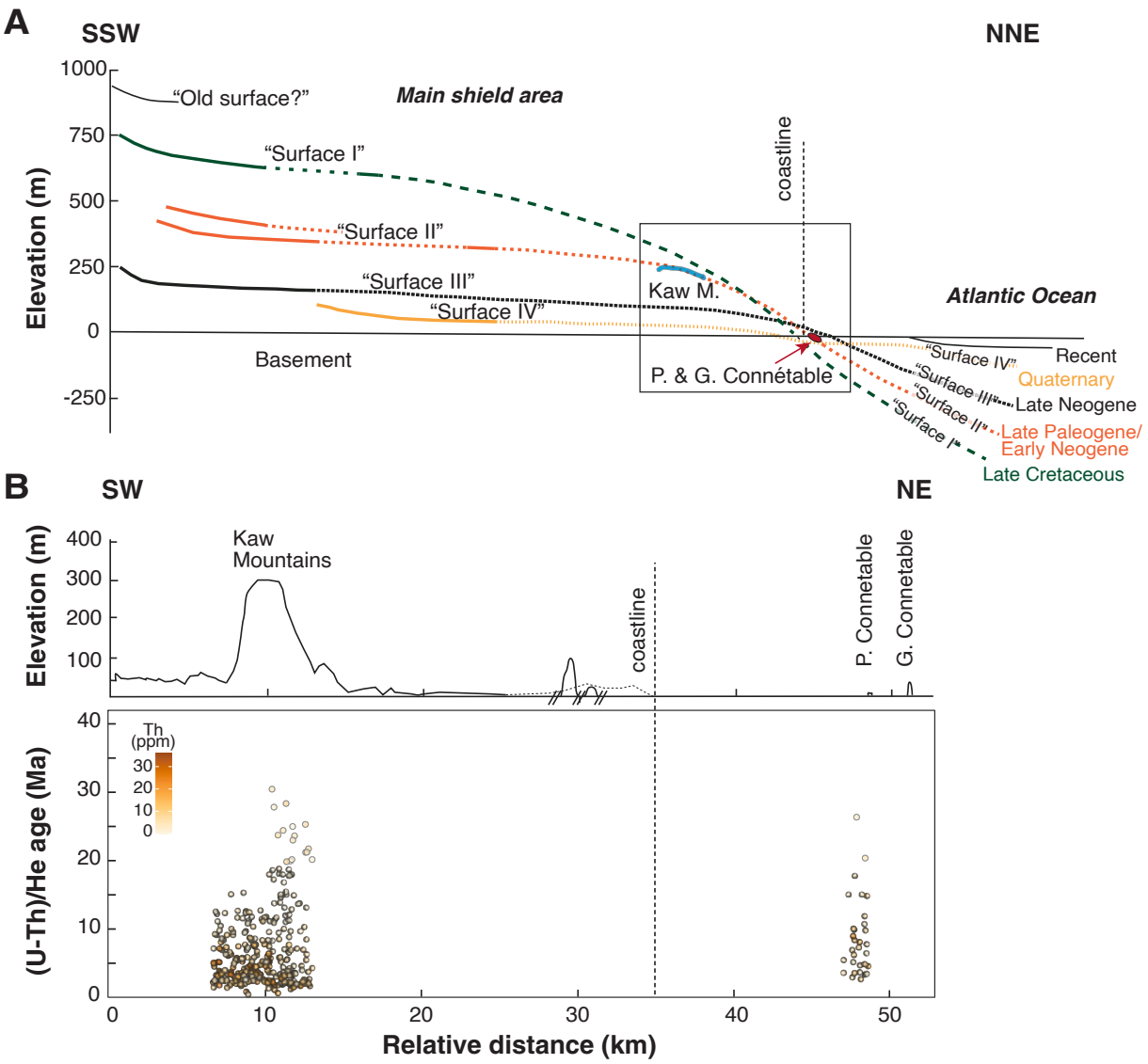

Fig. 11. (A) Geomorphological model of the Guiana shield from McConnell (1968) and Blancaneaux (1981) with the planation surfaces proposed for the Guianas, with proposed ages. Elevations are strongly exaggerated. (B) shows a schematic cross section from Kaw to Connétable. Obtained ages including those from Heller et al. (2022) are represented for the Connétable site. Note that for better visualization the data is plotted with a gentle x-spread and ages at Kaw were plotted separately for the northern and southern flank. Colour of the datapoints relates to Th concentration which tends to be higher for bauxitic subsamples.

simplified reading "higher elevation = older age", possibly true for the central areas of the shield, is probably not valid for coastal areas. McConnell (1968) proposes the existence of a coastal monocline where the different surfaces converge and are eventually inverted (Fig. 11). This means on the one hand that "old planation surfaces" might occur at much lower elevations near the coast and on the other hand that planation surfaces of different ages might have similar elevations near the coast. The weathering ages show that a Quaternary age for low elevation such as Connétable Islands, as proposed by Choubert (1957) and Blancaneaux (1981), is not possible because weathering traces back to the Miocene and Oligocene. However, the data is in concordance with the existence of a coastal monocline, as proposed by (McConnell, 1968), where the surfaces converge near the coast and similar ages occur at different elevations (Fig. 11). Whether the proposed geomorphological models and peneplanation surface ages are valid for the central areas of the Guiana shield cannot be decided from our data.

Indeed, the onset of lateritization at the Connétable Islands at ~30 Ma (Fig. 8) indicates that the landscape has undergone weathering since that time, regardless of elevation, as similar weathering conditions has also occurred at the Kaw Mountain site, which is located at 300 m a.s.l. These data enable us to demonstrate that the age-elevation correlations for paleosurfaces are much more complex than was previously suggested. Rather, our data demonstrate that the paleoclimatic conditions along the Atlantic coast of French Guiana and Suriname permitted the development of ferruginous laterites during the Oligo-Miocene, followed by a bauxitization event in the late Neogene associated with different drainage and/or more humid climatic conditions (this study; Ansart et al., 2022; Heller et al., 2022).

5.5. *Geological evolution of the Grand and Petit Connétable: A geological heritage perspective*

All the data acquired in this study allow us to reconstruct the geological formation and evolution of the Grand and Petit Connétable Islands over time, and help us to establish a of geological heritage database for their preservation. Firstly, laterization and bauxitization are weathering processes that depend on the presence of an aquifer; the latter cannot be preserved on islands as small as the Grand and Petit Connétable, since infiltrated water quickly runs off the sea. Therefore, it can be argued that the weathering processes of laterization and

bauxitization occurred only before the formation of the Grand and Petit Connétable islands, and that the islands are therefore younger than 2–3 Ma, as evidenced by the youngest (U–Th)/He age observed on the Petit Connétable. Given that alumino-phosphate minerals result from the reaction of guano-derived phosphoric acid and gibbsite, we can infer that the alumino-phosphate are younger than 2–3 Ma, i.e. when the gibbsite was formed and that bird colonies were established on the islands. However, this phenomenon could be much younger, as the birds may have settled after the last glacial maximum around 20,000 years ago when the sea level gradually rose from −130 m to its current level, favouring the formation of these islands (Antoine et al., 2024).

Direct evidence for the timing of bird colonization is lacking, but we infer that marine birds colonised the area only after 2–3 Ma (i.e., that there had been no guano in the area before it became an island), based on the fact that seabirds are much safer on islands (fewer predators) and face no offshore barriers (unlike onshore). It can therefore be suggested that the guano was brought to the area after the GC became an island, and after the formation of the bauxite profile; meaning that it had no impact on enhancing the weathering processes. The laterization of the GC and PC regions therefore occurred in the Oligocene, the bauxitization processes began in the Late Miocene and the duricrust formation processes ceased at 2–3 Ma, when the GC and PC sites were isolated from the mainland by the sea. However, during the Pleistocene glacial and interglacial cycles, the sea level changed significantly. Indeed, during the MIS-5 high stand ca 120,000 yr BP, the sea level was higher (Antoine et al., 2024), which would have submerged the PC island, and perhaps eroded its upper part. However, the geochemical data show no evidence of enrichment associated with the dissolution of marine shell debris (Tables 1, 2), and the data from this study provide non information on this time period. In addition, during the Pleistocene glacial period, the sea level was lower, and during that time, the GC and PC were connected. However, the (U-Th)/He geochronological data did not reveal this period. At some point after this, the GC was colonised by marine birds, whose guano mineralised to form phosphoric acid. This acid infiltrated almost all the saprolite and interacted with the gibbsite bauxite to form the aluminium phosphate deposit. This deposit was extracted in 1882, resulting in the current geomorphology of the GC Island. Fig. 12 summarises the geological history of Grand Connétable Island since the Oligocene in three main stages, based on mineralogical, geochemical and geochronological data obtained in this study.

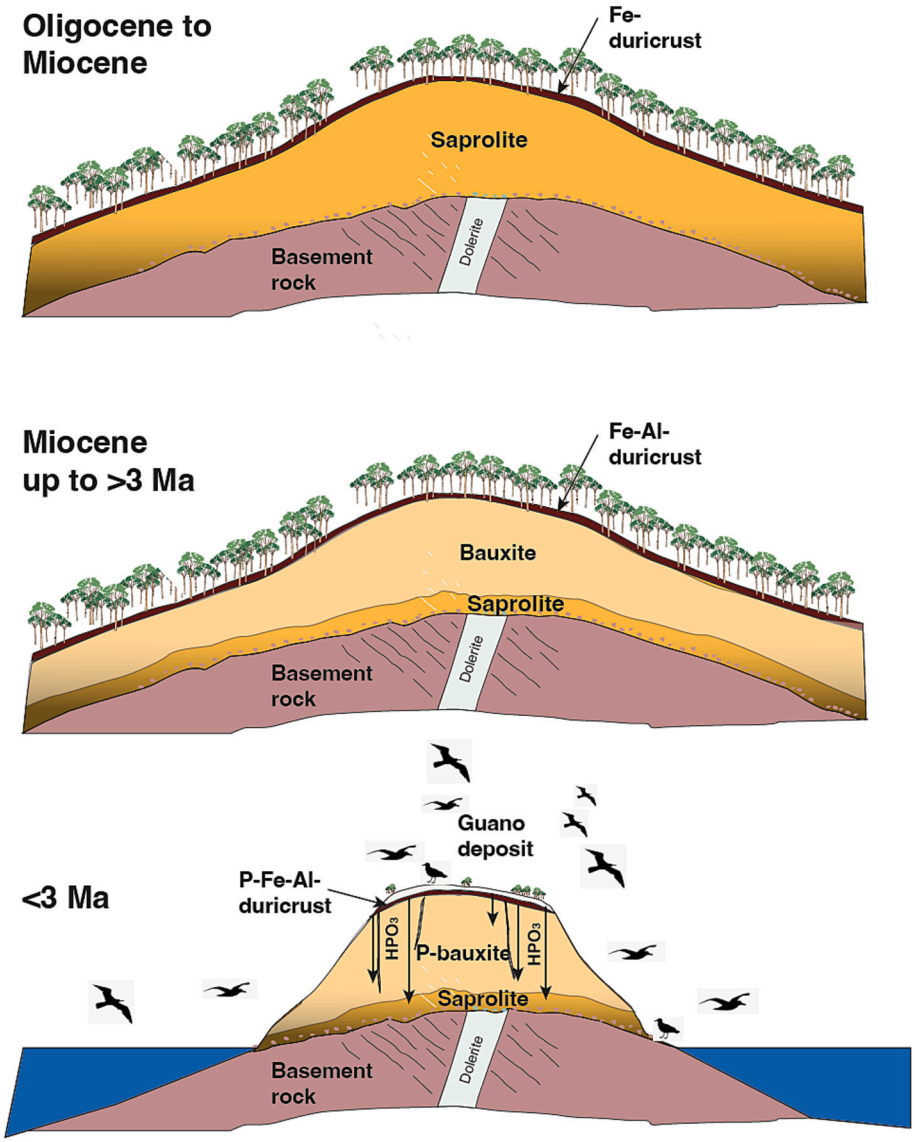

Fig. 12. A schematic reconstruction of the evolution of the Grand Connétable Island is presented in three steps, based on the mineralogical, geochemical and geochronological data obtained in this study. Oligocene to Miocene; Miocene up to >3 Ma and <3 Ma. Quaternary sea-level oscillations are not represented here.

6. Conclusions

Combining mineralogical, geochemical and geochronological methods enables us to shed light on the evolution of the Connétable islands and its distinctive phosphorus deposit. Hematite and goethite (U-Th)/He data from the PC duricrust indicate that GC and PC underwent laterization and bauxitization processes between 30 and 2 Ma, prior to the formation of the islands. The new data provide an important new dataset for discussing geomorphological models, as we demonstrate that the Kaw Mountains, located on the mainland coast, and the Connétable Islands have undergone strong weathering conditions since at least the Oligocene, regardless of elevation. This resulted in a weathering profile >35 m thick dominated by gibbsite bauxite profile (>30 m) suggesting more intense weathering at GC and PC than at the Kaw Mountain site. The presence of anorthosite-like bedrock may be an important factor in permitting more intense weathering and the formation of a thick bauxite profile at Grand Connétable. As with other weathering profiles, GC regolith samples are depleted in alkalis and alkali earths, and enriched in immobile elements present in the form of supergene minerals, namely gibbsite for Al (and kaolinite in a lesser extend), hematite (and occasionally goethite) for Fe. The evolution of the REE concentrations evolution within the bauxitic profile of the GC and PC is similar to that of bauxite in French Guiana and Suriname, suggesting similar weathering processes. The general enrichment of LREE and HREE depletion, especially in the upper part of the bauxitic profile at GC, reflects the impact of bauxite weathering in fractionating the REE. Finally, the aluminium, iron and titanite phosphate minerals are supergene, resulting from the reaction of phosphoric acid originating from marine birds' guano- and gibbsite and sulphate minerals. The formation of the Grand Connétable Island <3 Ma encouraged the development of bird colonies and sea water spray on the island.

7. Declaration of generative AI in scientific writing

The authors declare that they have not used any type of artificial intelligence (AI) and AI-assisted technologies in the writing process.

Author contributions

J.I., C.G., and A.H. contributed to project planning. J.I., C.G., A.H., G. A., A.C., F.L. and S.S. contributed to field survey and sampling. J.I., C.G., E.J., B.H., R.P.-J., T.A., S.C. and S.S. contributed to the mineralogical, geochemical and petrological and (U-Th)/He, analysis. C.G. and A.H. contributed to financial support. All authors contributed to manuscript and figures preparation.

Declaration of competing interest

The authors declare that they have no known competing financial interests or personal relationships that could have appeared to influence the work reported in this paper.

Acknowledgment

This work was funded and carried out in the framework of the French funding Agency ANR RECA-ANR-17-CE01-0012-01 project. F. Haurine, S. Denti and N. Findling are warmly thanked for the ICP-MS, sample preparation and XRD analysis. The Reserve Naturelle Nationale du Grand Connétable staff is also warmly thanked for their help in the organization of the sampling mission as well as M. Lanson, from BRGM, for their help during the first sampling mission. Anonymous reviewer and Huayong Chen editor are warmly thanked for their constructive comments.

Appendix A. Supplementary data

Supplementary data to this article can be found online at https://doi.org/10.1016/j.oregeorev.2026.107280.

Data availability

Data will be made available on request.

References

Aleva, G.J.J., 1984. Lateritization, bauxitization and cyclic landscape development in the Guiana Shield. In: Jacob Jr, L. (Ed.), Bauxite. A.I.M.E, New York, USA, pp. 297–318.
Ansart, C., Quantin, C., Calmels, D., Allard, J., Roig, J.-Y., Couëffe, R., Heller, B., Pinna Jamme, R., Nouet, J., Reguer, S., Vantelon, D., Gautheron, C., 2022. (U-Th)/He Geochronology Constraints on Lateritic Duricrust Formation on the Guiana Shield. Front. Earth Sci. 10, 888993.
Antoine, P.O., Wieringa, L.N., Adnet, S., Aguilera, O., Bodin, S.C., Cairns, S., Conejeros-Vargas, C.A., Cornée, J.-J., Eżerinskis, Z., Fietzke, J., Gribenski, N.O., Grouard, S., Hendy, A., Hoorn, K., Joannes-Boyau, R., Langer, M.R., Luque, J., Marivaux, L., Moissette, P., Nooren, K., Quillévéré, F., Šapolaitė, J., Sciumbata, M., Valla, P.G., Witteveen, N.H., Casanova, A., Clavier, S., Bidgrain, P., Gallay, M., Rhoné, M., Heuret, A., 2024. A Late Pleistocene coastal ecosystem in French Guiana was hyperdiverse relative to today. PNAS 121, e2311597121.
Bardossy, G. and Aleva, G.J.J. (1990) Lateritic bauxites.
Basile, C., Mascle, J., Guiraud, R., 2005. Phanerozoic geological evolution of the Equatorial Atlantic domain. J. Afr. Earth Sc. 43, 275–282.
Bassal, F., Heller, H., Roques, J., Balout, H., Tassan-Got, L., Allard, T., Gautheron, C., 2022. Revealing the radiation damage and Al-content impacts on He diffusion in goethite. Chem. Geol. 611, 121118.
Berger, A., Janots, E., Gnos, E., Frei, R., Bernier, F., 2014. Rare earth element mineralogy and geochemistry in a laterite profile from Madagascar. Appl. Geochem. 41, 218–228.
Best, M. (2003) Igneous and metamorphic petrology.
Blancaneaux, P., 1981. Essai sur le milieu naturel de la Guyane Française. Trav. Doc. ORSTOM. ORSTOM 341.
Carozzi, A.V., 1979. Petroleum geology in the Paleozoic clastics of the Middle Amazon Basin, Brazil. J. Pet. Geol 2, 55–74.
Cautru, J.P., Marteau, P., Tostain, O., Joseph, B., 1998. Reconnaissance géologique de l'île du Grand Connétable. Rapport BRGM.
Choubert, B. (1957) Essai sur la géomorphologie de la Guyane. , in: Mémoire, C.g.d.d.l.F. D.d.l.G.I.N. (Ed.), Paris, 43 pp.
Cushman, G.T. (2013) Guano and the opening of the Pacific world: a global ecological history.
Delor, C., Lahondere, D., Egal, E., Lafon, J.-M., Cocherie, A., Guerrot, C., Rossi, P., Truffert, C., Théveniaut, H., Phillips, D., de Avelar, V.G., 2003. Transamazonian crustal growth and reworking as revealed by the 1: 500,000-scale geological map of French Guiana. Géologie De La France 2-3-4, 5–57.
Derycke, A., Gautheron, C., Barbarand, J., Bourbon, P., Aertgeerts, G., Simon-Labric, T., Sarda, P., Pinna Jamme, R., Boukari, C., Haurine, F., 2021. French Guiana margin evolution: from Gondwana accretion to Atlantic opening. Terra Nova 33, 415–422.
Dill, G.H., 2000. The geology of aluminium phosphates and sulfates of the alunite group minerals: a review. Earth Sci. Rev. 53, 35–93.
Eglinger, A., André-Mayer, A.-S., Combes, V., Teitler, Y., Heuret, A., 2020. Les gisements d'ord de la Guyane Française. Géologues 206, 36–40.
Foord, E.E., Taggart, J.E., 1986. A reexamination of the turquoise group: the mineral aheylite, planerite (redefined), turquoise and coeruleolactite. Mineral. Mag. 62, 93–111.
Gautheron, C., Pinna Jamme, R., Derycke, A., Ahadi, F., Sanchez, C., Haurine, F., Monvoisin, G., Barbosa, D., Delpech, G., Maltese, J., Sarda, P., Tassan-Got, L., 2021. Technical note: Analytical protocols and performance for apatite and zircon (U–Th)/He analysis on quadrupole and magnetic sector mass spectrometer systems between 2007 and 2020. Geochronology 3, 351–370.
Grahn, Y., Caputo, M.V., 1992. Early Silurian glaciations in Brazil. Palaeogeogr. Palaeoclimatol. Palaeoecol. 99, 9–15.
Han, J., Kamber, M. and Pei, J. (2011) Data Mining Concepts and Techniques, Third edition.
Heller, B.M., 2022. Temporal evolution of Amazonian laterites reconstructed from mineralogy, geochemistry and geochronology. GEOPS-IMPMC. Université Paris-Saclay and Sorbonne Université.
Heller, B.M., Bressan-Riffel, S., Allard, T., Morin, G., Roig, J.-Y., Couëffe, R., Aertgeerts, G., Derycke, A., Ansart, C., Pinna Jamme, R., Gautheron, C., 2022. Reading the climate signals hidden in bauxite. Geochim. Cosmochim. Acta 323, 40–73.
King, L.C., 1962. Morphology of the Earth. Oliver and Boyd Publ. House, London.
Kiratisin, A., Demaille, D., 2006. XIX. Les perles en variscite d'Er Grah. Gallia Préhistoire 38, 205–223.
Kroonenberg, S., Mason, P.R.D., Kriegsman, L., de Roever, E.W.F., Wong, T.E., 2019. Geology and mineral deposits of the Guiana Shield. Mededeling Geologisch Mijnbouwkundige Dienst Suriname 29, 111–116.
Lindsay, W.L., Vlek, P.L., Chien, S.H., 1989. Phosphate minerals. Min. Soil Environ. 1, 1089–1130.

Longueville, F., Aertgeerts, G. and Lanson, M. (2021) Géologie structurale et cartographie des fonds marins des îles de la réserve du Grand-Connétable en Guyane. BRGM/RP-71163-FR, p. 58.
Marzoli, A., Callegaro, S., Dal Corso, J., Davies, J.H.F.L., Chiaradia, M., Youbi, N., Bertrand, A., Reisberg, L., Merle, E., Jourdan, F., 2017. The Central Atlantic magmatic province (CAMP): a review. In: Tanner, L. (Ed.), The Late Triassic World. Topics in Geobiology. Springer.
Matsubara, S., Kato, A., 1994. Aluminum Phosphates from Inokura, Imaichi City, Tochigi Prefecture, Japan. Bull. Natl. Sci. Museum: Geol. Paleontol. Series C 20, 79–88.
Matsubara, S., Saito, Y., Kato, A., 1988. Phosphate minerals in chert from Toyoda, Kochi, City, Japan. J. Min. Petro. Econ. Geol. 83, 141–149.
McConnell, R.B., 1968. Planation Surfaces in Guyana. Geogr. J. 134, 506–520.
McCusker, L.B., Von Dreele, R.B.E., C.D., Louer, D., Scardi, P., 1999. Rietveld refinement guidelines. J. Appl. Cryst. 32, 36–50.
McDonough, W.F., Sun, S., 1995. The composition of the Earth. Chem. Geol. 120, 223–253.
Monsels, D.A., Van Bergen, M.J., 2017. Bauxite formation on Proterozoic bedrock of Suriname. J. Geochem. Explor. 180, 71–90.
Monsels, D.A., Van Bergen, M.J., 2019. Bauxite formation on Tertiary sediments in the coastal plain of Suriname. J. South Am. Earth Sci. 89, 275–298.
Nahon, D., Tardy, Y., 1992. Chapter I.3 - the Ferruginous Laterites. Handb. Explor. Geochem. 4, 41–55.
Nomade, S., Pouclet, A., Chen, Y., 2002. The French Guyana doleritic dykes: geochemical evidence of three populations and new data for the Jurassic Central Atlantic Magmatic Province. J. Geodyn. 34, 595–614.
Rostan, P., 2011. La Ruée vers les phosphates. Une Saison En Guyane 6, 66–68.
Rostan, P., 2013. Les Vestiges Miniers de l'île du Grand Connétable, Commune de Régina. Karapa 2, 61–69.
Santana-Sagredo, F., Schulting, R.J., Méndez-Quiros, P., Vidal-Elgueta, A., Uribe, M., Loyola, R., Maturana-Fernández, A., Díaz, F.P., Latorre, C., McRostie, V.B., Santoro, C.M., Mandakovic, V., Harrod, C., Lee-Thorp, J., 2021. 'White gold'guano fertilizer drove agricultural intensification in the Atacama Desert from AD 1000. Nat. Plants 7, 152–158.
Sapin, F., Davaux, M., Dall'Asta, M., Lahmi, M., Baudot, G., Rigenbach, J.-C., 2016. Post-rift subsidence of the French Guiana hyper-oblique margin: from rift-inherited subsidence to Amazon deposition effect. Geol. Soc., London 431, 125–144.
Schnug, E., Jacobs, F., Stöven, K., 2018. Guano: the white gold of the seabirds. Seabirds 1, 79–100.
Skaggs, J. (1994) The Great Guano Rush: Entrepreneurs and American Overseas Expansion, ISBN 978-0-312-10316-3 ed, New York.
Tardy, Y. (1992) Pétrologie des latérites et des sols tropicaux. Vol. 459. Paris: Masson.
Théveniaut, H., Delor, C., Lafon, J.-M., Monié, P., Rossi, P., Lahondère, D., 2006. Paleoproterozoic (2155–1970 Ma) evolution of the Guiana Shield (Transamazonian event) in the light of new paleomagnetic data from French Guiana. Precambr. Res. 150, 221–256.
Théveniaut, H., Freyssinet, P., 1999. Paleomagnetism applied to lateritic profiles to assess saprolite and duricrust formations processes: the example of Mont Baduel profil (French Guiana). Palaeo 148, 209–231.
Théveniaut, H., Freyssinet, P., 2002. Timing of lateritization on the Guiana Shield: synthesis of paleomagnetic results from French Guiana and Suriname. Palaeogeogr. Palaeoclimatol. Palaeoecol. 178, 91–117.
Van der Hammen, T., Wymstra, T.A., 1964. A palynological study on the Tertiary and Upper cretaceous of British Guiana. Leidse. Geol. Meded. 30, 183–214.
Vanderhaeghe, O., Ledru, P., Thiéblemeont, D., Egal, E., Cocherie, A., Tegyey, M., Milesi, J.P., 1998. Contrasting mechanism of crustal growth Geodynamic evolution of the granite-greenstone belts of French Guiana. Precamb. Res. 85, 1–25.
Verhaert, M., Gautheron, C., Dekoninck, A., Vennemann, V., Pinna Jamme, R., Mouttaqi, A., Yans, J., 2022. Unravelling the Temporal and Chemical Evolution of a mineralizing Fluid in Karst-Hosted deposits: a Record from Goethite in the High Atlas Foreland (Morocco). Minerals 12, 1151.
Warr, L.N., 2021. IMA–CNMNC approved mineral symbols. Mineralogical Magazine 85 (3), 291–320.
Weill, D.F., Drake, M.J., 1973. Europium anomaly in plagioclase feldspar: experimental results and semiquantitative model. Science 180, 1059–1060.
Wiggenhauser, M., Aucour, A.M., Bureau, S., Campillo, S., Telouk, P., Romani, M., Ma, J. F., Landrot, G., Sarret, G., 2021. Cadmium transfer in contaminated soil-rice systems: Insights from solid-state speciation analysis and stable isotope fractionation. Environ. Pollut. 269, 115934.
Wong, T.E., 1994. The Paleocene-Eocene succession in the Guiana basin. Bulletin De La Société Belge De Géologie 103, 281–291.